

# Polarization flare of 3C 454.3 at millimeter wavelengths seen from decadal polarimetric observations

Hyeon-Woo Jeong<sup>1,2</sup>, Sang-Sung Lee<sup>1,2\*</sup>, Sincheol Kang<sup>2</sup>, Minchul Kam<sup>3,4</sup>, Sanghyun Kim<sup>1,2</sup>,  
Whee Yeon Cheong<sup>1,2</sup>, Do-Young Byun<sup>1,2</sup>, Chanwoo Song<sup>1,2</sup>, and Sascha Trippe<sup>4,5</sup>

<sup>1</sup> Astronomy and Space Science, University of Science and Technology, 217 Gajeong-ro, Yuseong-gu, Daejeon 34113, Republic of Korea

<sup>2</sup> Korea Astronomy and Space Science Institute, 776 Daedeok-daero, Yuseong-gu, Daejeon 34055, Republic of Korea

<sup>3</sup> Institute of Astronomy and Astrophysics, Academia Sinica, PO Box 23-141, Taipei 10617, Taiwan

<sup>4</sup> Department of Physics and Astronomy, Seoul National University, Gwanak-gu, Seoul 08826, Republic of Korea

<sup>5</sup> SNU Astronomy Research Center, Seoul National University, Gwanak-gu, Seoul 08826, Korea

Received 19 November 2024 / Accepted 27 February 2025

## ABSTRACT

**Context.** The blazar 3C 454.3 ( $z = 0.859$ ) has been extensively investigated using multiwavelength high-resolution polarization studies, showing polarization variations on milliarcsecond scales.

**Aims.** This study investigates the polarimetric characteristics of the blazar 3C 454.3 at 22–129 GHz using decadal (2011–2022) data sets. In addition, we also delve into the origin of the polarization flare observed in 2019.

**Methods.** The corresponding data sets were obtained from the single-dish mode observations of the Korean VLBI Network (KVN) and the 43 GHz Very Long Baseline Array (VLBA). Using those data, we compared the consistency of the measurements between milliarcsecond and arcsecond scales. The Faraday rotation measure (RM) values were obtained via two approaches: model fitting to a linear function in all frequency ranges and calculating from adjacent frequency pairs.

**Results.** We found that the preferred linear polarization angle is  $\sim 100^\circ$  when the source is highly polarized, for example during a flare. At 43 GHz we found that the polarized emission at of milliarcsecond and arcsecond scales is consistent when we compare its flux density and polarization angle. The ratio of quasi-simultaneously measured (within a week) polarized flux density is  $1.02 \pm 0.07$  (i.e.,  $\Delta S_p/S_p \approx 2\%$ ) and the polarization angles display similar rotation, which suggest that the extended jet beyond the scale of VLBA 43 GHz has a negligible convolution effect on the polarization angle from the KVN. We found an interesting and notable flaring event in the KVN single-dish data from the polarized emission in 2019 in the frequency range of 22–129 GHz. During the flare, the observed polarization angles ( $\chi_{\text{obs}}$ ) rotate from  $\sim 150^\circ$  to  $\sim 100^\circ$  at all frequencies with a chromatic polarization degree ( $m_p$ ).

**Conclusions.** Based on the observed  $m_p$  and  $\chi_{\text{obs}}$ , and also on the Faraday rotation measure, we suggest that the polarization flare in 2019 is attributed to the shock–shock interaction in the stationary jet region. The change in the viewing angle of the jet alone is insufficient to describe the increase in brightness temperature, indicating the presence of source intrinsic processes such as particle acceleration.

**Key words.** polarization – galaxies: active – galaxies: jets – radio continuum: galaxies – quasars: individual: 3C 454.3

## 1. Introduction

Blazars are a subclass of active galactic nuclei (AGNs) in which a relativistic jet is inclined with a small viewing angle between the jet and the line of sight. The small viewing angle of the jet enhances the Doppler boosting effects, leading to rapid variability. The jet emits radiation over the entire range of electromagnetic waves, which is dominated by synchrotron radiation from radio to optical bands, and radiation by inverse-Compton scattering in higher energy bands (e.g.,  $\gamma$ -rays). Synchrotron radiation is emitted by relativistic electrons gyrating around magnetic field lines in the jet.

The synchrotron radiation from the relativistic jets is most likely polarized, with its polarized properties strongly constrained by magnetic field environments in the jet. If the field lines in the jets are well ordered and strong, a high degree of linear polarization ( $m_p$ ) and high polarized flux density ( $S_p$ ) can be observed. Theoretically, for an ideal case (i.e., a perfectly

ordered magnetic field),  $m_p$  reaching up to  $\sim 75\%$  is feasible for electrons having power-law energy distribution in an optically thin (e.g.,  $\alpha = -1$ , where  $S \propto \nu^\alpha$ ) region (Rybicki & Lightman 1979; Trippe 2014). Meanwhile, for an optically thick region, the observed  $m_p$  is expected to decrease (e.g., by only a few percent of  $m_p$ ).

In addition, observational results have identified polarized emission from AGN, and both  $m_p$  and the polarization angle ( $\chi$ ) seem to give information about the magnetic field lines in a jet. Several studies have reported the results of polarization observations in both radio and optical bands for AGNs and found highly polarized emission reaching a few tens of percent in polarization degree (Jorstad et al. 2005, 2007; Pushkarev et al. 2023). As the optically thick region is believed to have low  $m_p$ , even with perfectly ordered magnetic field lines, this implies an optically thin polarized emission from some AGNs at high radio frequency (e.g.,  $\gtrsim 86$  GHz), since optical wavelengths are optically thin by default. Angelakis et al. (2016) suggested a model discriminating between low- and high-synchrotron peak (LSP

\* Corresponding author: sslee@kasi.re.kr

and HSP, respectively) blazars based on the optical polarimetry (see also [Blinov & Pavlidou 2019](#)). In their work, at optical wavelengths it seems that LSP blazars exhibit highly polarized emission with a random  $\chi$  distribution and opposite characteristics (i.e., a low degree of polarization with a specific  $\chi$ ) for HSP blazars.

Recently, at shorter wavelengths, the Imaging X-ray Polarimetric Explorer (IXPE) has been observing polarized emission X-rays from celestial objects, including AGNs, and has identified jet models of the AGNs by comparison with radio and optical polarization behavior ([Di Gesu et al. 2022](#); [Marinucci et al. 2022](#); [Liodakis et al. 2022](#); [Middei et al. 2023a](#); [Peirson et al. 2023](#); [Middei et al. 2023b](#); [Kim et al. 2024](#)). Among the X-ray studies, the highest measurement in  $m_p$  is about 22%. However, we note that the polarization degrees listed above are not representative values at each observing frequency since the samples and observing periods are different from each other.

Although the observed polarization angle  $\chi_{\text{obs}}$  most likely provides us with information about the orientation of magnetic field lines in the jet, the Faraday effect contaminates the intrinsic polarized emission when the emission propagates through an ionized medium with magnetic field lines ([Burn 1966](#); [Sokoloff et al. 1998](#)). This leads to a rotation of  $\chi$ , which is proportional to the squared wavelength,  $\Delta\chi \propto \text{RM} \lambda^2$ , where  $\Delta\chi = \chi_{\text{obs}} - \chi_0$  (with  $\chi_0$  is the intrinsic polarization angle). The observed polarization angle can then be written in the form of  $\chi_{\text{obs}} = \chi_0 + \text{RM} \lambda^2$ , where  $\chi_{\text{obs}}$  is the observed polarization angle and  $\lambda$  is the observing wavelength. RM is the Faraday rotation measure, indicating the amount of rotation in the polarization angle by a medium in units of  $\text{rad m}^{-2}$ . Therefore, the Faraday rotation is larger at longer wavelengths. Based on this expression, we can calculate the RM as  $\text{RM} = (\chi_1 - \chi_2)/(\lambda_1^2 - \lambda_2^2)$ , where  $\chi_1$  and  $\chi_2$  are the observed polarization angles at wavelengths  $\lambda_1$  and  $\lambda_2$ , respectively. For a cosmological source at redshift  $z$ , RM is defined as

$$\text{RM} = \frac{e^3}{2\pi m_e^2 c^4} \frac{1}{(1+z)^2} \int n_e(l) B_{\parallel}(l) dl, \quad (1)$$

where  $m_e$  and  $e$  are the mass and charge of an electron,  $c$  is the speed of light,  $n_e$  is the electron number density of a Faraday screening medium,  $B_{\parallel}$  is the magnetic field strength along the line of sight, and  $l$  is the path length through the medium where the Faraday rotation takes place.

At millimeter wavelengths, the Institute for Radio Astronomy in the Millimeter Range (IRAM) 30 m radio telescope has monitored 37 AGNs at 86 and 229 GHz ([Agudo et al. 2018a](#)) in dual-polarization mode to investigate the linear polarization variability of the AGNs ([Agudo et al. 2018b](#)). In their work, they found faster variability and larger fractional linear polarization at 229 GHz than at 86 GHz.

The sign of RM depends on  $B_{\parallel}$  to the line of sight, as indicated in Equation (1). A few multiwavelength polarization studies have revealed high absolute RM ( $|\text{RM}|$ ) values of  $\sim 10^5 \text{ rad m}^{-2}$  in the observer's frame (e.g., [Kuo et al. 2014](#); [Park et al. 2018](#); [Agudo et al. 2018b](#); [Hovatta et al. 2019](#)). In the Atacama Large Millimeter Array (ALMA) observations, a higher order of  $|\text{RM}|$  ( $\sim 10^7 \text{ rad m}^{-2}$  in observer frame) was found from a gravitationally lensed AGN called PKS 1830–211 at 250–300 GHz pair ([Martí-Vidal et al. 2015](#)). This was attributed to high  $n_e$  and/or strong  $B_{\parallel}$  of the screening medium (see Equation (1) in their work).

The blazar 3C 454.3 ( $z = 0.859$ ) has been extensively investigated in multiwavelength high-resolution polarization

studies. In very long baseline interferometry (VLBI) observations at 15 GHz, the source was resolved with a widely extended jet structure beyond  $\sim 10$  mas from the central engine, ejecting toward the northwest side ([Lister et al. 2018, 2021](#); [Pushkarev et al. 2023](#)). At 43 GHz, two prominent regions have been identified over a decade: the core and a quasi-stationary component (0.45–0.70 mas away from the core, hereafter, Region C, [Jorstad et al. 2017](#); [Weaver et al. 2022](#)). Typically, Region C exhibits a higher polarization degree than that of the core with a stable polarization angle aligned to  $\sim 90^\circ$  (an east-west direction, [Kemball et al. 1996](#); [Jorstad et al. 2005, 2013](#); [Traianou et al. 2024](#)). Based on its observed properties, including re-brightening, decrease in the angular size of the jet, and spatial stationariness ([Gómez et al. 1999](#); [Jeong et al. 2023](#)), Region C was suggested as a recollimation shock. For a downstream region, [Zamaninasab et al. \(2013\)](#) found a large-scale helical magnetic field structure in 3C 454.3 by comparing the predictions of the helical jet model and observed polarimetric properties across the jet, using the multifrequency Very Long Baseline Array (VLBA<sup>1</sup>) observations.

Several studies were conducted to evaluate magnetic field strength in the jet of 3C 454.3. Based on the core-shift effect, the magnetic field strengths at the 43 GHz core and 1 pc from the central engine were found to be in 0.03–0.11 G and 0.2–1.13 G, respectively, within  $1\sigma$  uncertainty ([Pushkarev et al. 2012](#); [Kutkin et al. 2014](#); [Mohan et al. 2015](#); [Chamani et al. 2023](#)). In addition, [Jeong et al. \(2023\)](#) estimated magnetic field strengths of the optically thick ( $\tau = 1$ ) surface in the jet via the synchrotron self-absorption (SSA) effect. They found two distinctive SSA components, LSS and HSS (LSS: lower turnover frequency SSA spectrum and HSS: higher turnover frequency SSA spectrum; for more details, see Figure 4 and the text in [Jeong et al. 2023](#)), which have turnover frequencies at the low-frequency ( $\lesssim 30$  GHz) and high-frequency ( $\gtrsim 60$  GHz) range. The estimated magnetic field strengths of the HSS were in the range of 0.1–7 mG. The LSS identified before the  $\gamma$ -ray flare in June 2014 ([Buson 2014](#)) corresponds to Region C, and they found a magnetic dominance based on a higher SSA magnetic field strength than that in the equipartition condition.

For this study we investigated the decadal polarimetric characteristics of the source using the simultaneous multifrequency (22–129 GHz) single-dish observations from the Korean VLBI Network (KVN<sup>2</sup>). We also employed the data from the 43 GHz VLBA, managed by the Boston University (BU<sup>3</sup>) group. The obtained VLBA data were used for comparison with the KVN data at 43 GHz and to resolve the source structure. The data sets used in this study have a time range from 2011–2022, and several  $\gamma$ -ray activities were reported in this period ([Buson 2014](#); [Jorstad et al. 2015](#); [Ojha 2016](#); [Panebianco et al. 2022](#)). The observations included in this study will be described in Section 2. The variability of the arcsecond-scale structure observed by the KVN single-dish and the variability of the milliarcsecond-scale structures resolved by the VLBA are shown in Section 3.1. We investigated the Faraday rotation measure using the KVN observations in Section 3.2. In Section 4 we discuss the observed features in the core and Region C. Our conclusions and a summary of this work are presented in Section 5.

<sup>1</sup> <https://science.nrao.edu/facilities/vlba>

<sup>2</sup> <https://radio.kasi.re.kr/kvn/main.php>

<sup>3</sup> <https://www.bu.edu/blazars/BEAM-ME.html>

## 2. Observations and data reduction

### 2.1. The KVN single-dish

MOGABA (MONitoring of GAMMA-ray Bright Active galactic nuclei; Kang et al. 2015) is one of the polarimetric monitoring programs using the KVN on AGNs through the single-dish mode. Another monitoring program, PAGaN (Plasma-physics of Active Galactic Nuclei; Park et al. 2018), has also been conducted for VLBI polarimetry, and their joint single-dish observation is used to calibrate the absolute polarization angle (Kam et al. 2023). 3C 454.3 is one of the target sources of MOGABA and PAGaN.

This work used polarimetric monitoring data in the time periods 2011–2022 (MOGABA) and 2016–2022 (PAGaN) from the KVN 21 m radio telescopes at 22, 43, 86, and 129 GHz on 3C 454.3 in single-dish mode; the corresponding beam sizes are approximately 133, 68, 34 and 23 arcseconds. The KVN consists of three identical 21 m antennas located in Seoul (KVN-Yonsei, KYS), Ulsan (KVN-Ulsan, KUS), and Jeju (KVN-Tamna, KTN); it has a unique capability of simultaneous four-frequency (22, 43, 86, and 129 GHz) observation in VLBI mode. In single-dish mode observation, two antennas were employed quasi-simultaneously (e.g., KTN at 22/43 GHz and KYS at 86/129 GHz). The polarimetric observables are recorded via the circularly polarized feed horns in the KVN receiver.

The polarimetric properties were measured using eight sets of position-switching scans with a bandwidth of 512 MHz after correcting antenna pointing via cross-scan observation. Several unpolarized sources, mainly planets in the Solar System (Venus, Mars, and Jupiter), were observed to measure and correct the polarization leakage term (called the D-term). We followed the data reduction pipeline introduced in Kang et al. (2015) to calibrate the KVN single-dish polarimetric data. The absolute polarization angle of the target sources from the MOGABA was obtained by considering the angle of the Crab nebula in intensity peak position,  $\chi_{\text{Crab}} = 152^\circ$  (Aumont et al. 2010; Weiland et al. 2011; Planck Collaboration XXVI 2016), at all frequencies (22–129 GHz). The quality of the obtained absolute polarization angle in a session was evaluated by comparing the angle of 3C 286 with the literature values (i.e.,  $33^\circ$ – $39^\circ$ , see Agudo et al. 2012, 2018a; Perley & Butler 2013; Hull & Plambeck 2015; Nagai et al. 2016). The absolute polarization angle of the PAGaN data was calibrated using the Crab nebula, but at slightly different reference angle (for more details, see Kam et al. 2023). The difference in reference angles between the two data sets is less than  $3^\circ$  at all frequencies, and in most cases, the difference is smaller than the uncertainties in  $\chi_{\text{obs}}$  of 3C 454.3 at all frequencies. Therefore, the difference in reference angle would not bias the results, so we used all the data together for further analysis.

The conversion of antenna temperature to flux density was performed by scaling the antenna temperature of the planets to their brightness temperature. For Jupiter, we referred to the brightness temperatures,  $T_{b,22} = 136.2 \pm 0.85$  and  $T_{b,43} = 155.2 \pm 0.87$  in units of Kelvin, at 22 and 43 GHz, respectively (Weiland et al. 2011). We did not use Jupiter for the scaling at 86 and 129 GHz because of the large angular size compared to the KVN beam sizes and its nonuniform brightness temperature distribution on its surface (de Pater et al. 2019). For Mars, we referred to the Mars brightness temperature modeling results at 43, 86, and 129 GHz from the open website<sup>4</sup>. In

Dahal et al. (2023) the brightness temperatures of Venus at various radio frequencies were compiled, and we referred to that data.

### 2.2. The VLBA 43 GHz

About 40 AGN sources have been monitored using the VLBA at 43 GHz by the BU group, and they studied jet kinematics using the monitoring data (Jorstad et al. 2017; Weaver et al. 2022). Polarimetric characteristics were also investigated by Jorstad et al. (2005). 3C 454.3 is one of the monitoring sources in the program. Thanks to the long baseline length of the VLBA, 3C 454.3 has been resolved into a compact radio core at the end of the east side with an extended jet structure in the north-eastern direction. A quasi-stationary component (Region C) that has a high polarization degree reaching up to a few tens of percent, has been reported. Recently, Traianou et al. (2024) studied milliarcsecond-scale characteristics on 3C 454.3 at 43 and 86 GHz, including polarimetry, between 2013 and 2017. In our work we utilized the 43 GHz VLBA data in the period from January 2011 to June 2022 to investigate the polarimetric characteristics of the source structures within the milliarcsecond-scale (such as the core and Region C) in a more extended period of time. We used the CLEAN algorithm (e.g., Högbom 1974; Clark 1980; Cornwell et al. 1999) for imaging and the modelfit task with circular Gaussian models in the DIFMAP software (Shepherd et al. 1997) to measure the respective locations of the radio core and Region C.

## 3. Results

### 3.1. Multifrequency variability

Figure 1 shows the light curves of 3C 454.3 obtained from the KVN single-dish at 22, 43, 86, and 129 GHz. From top to bottom, each panel shows the variation in the total flux density ( $S_I$ , Jy), linearly polarized flux density ( $S_p$ , mJy), polarization degree ( $m_p$ , %), and the observed polarization angle ( $\chi_{\text{obs}}$ ,  $^\circ$ ). In this study, we resolved the  $n\pi$ -ambiguity of  $\chi_{\text{obs}}$  in the frequency range of 22–129 GHz in both time and frequency. First, we resolved the  $n\pi$ -ambiguity of  $\chi_{\text{obs}}$  in time following Blinov et al. (2016) (see also Kiehlmann et al. 2016). In their methodology, they consider significant variation, for instance more than  $90^\circ$  between adjacent epochs as a consequence of the  $n\pi$ -ambiguity. Therefore, if  $\Delta\chi_t - \sqrt{\sigma_{\chi_{n+1}}^2 + \sigma_{\chi_n}^2} > 90^\circ$ , we resolved the  $n\pi$ -ambiguity in time, where  $\Delta\chi_t$  and  $\sigma_{\chi_n}$  are the amount of variation of  $\chi_{\text{obs}}$  within two adjacent epochs and uncertainty of the  $n$ th measurement, respectively. Then, similarly, we resolved the  $n\pi$  ambiguity across all the frequencies in the same epoch by using 22 GHz data as a reference, which has better cadence and sensitivity than other frequencies. A similar approach was employed by Agudo et al. (2018b) to resolve the  $n\pi$ -ambiguity of 3 mm and 1 mm data, but the authors used an angle difference between the smoothed angle from the previous two data points and the third data point among three data points. The mean cadence of the 22 GHz data in our study is about one month, and the overall percentage of uncertainties in total flux density were  $\sim 1.8\%$ ,  $\sim 1.6\%$ ,  $\sim 3.3\%$ , and  $\sim 9.3\%$  at 22, 43, 86, and 129 GHz, respectively. We note that the presented uncertainties are statistical errors. To consider the systematic errors from calibration, pointing offset to the source, and opacity correction,

<sup>4</sup> <https://lesia.obspm.fr/perso/emmanuel-lellouch/mars>

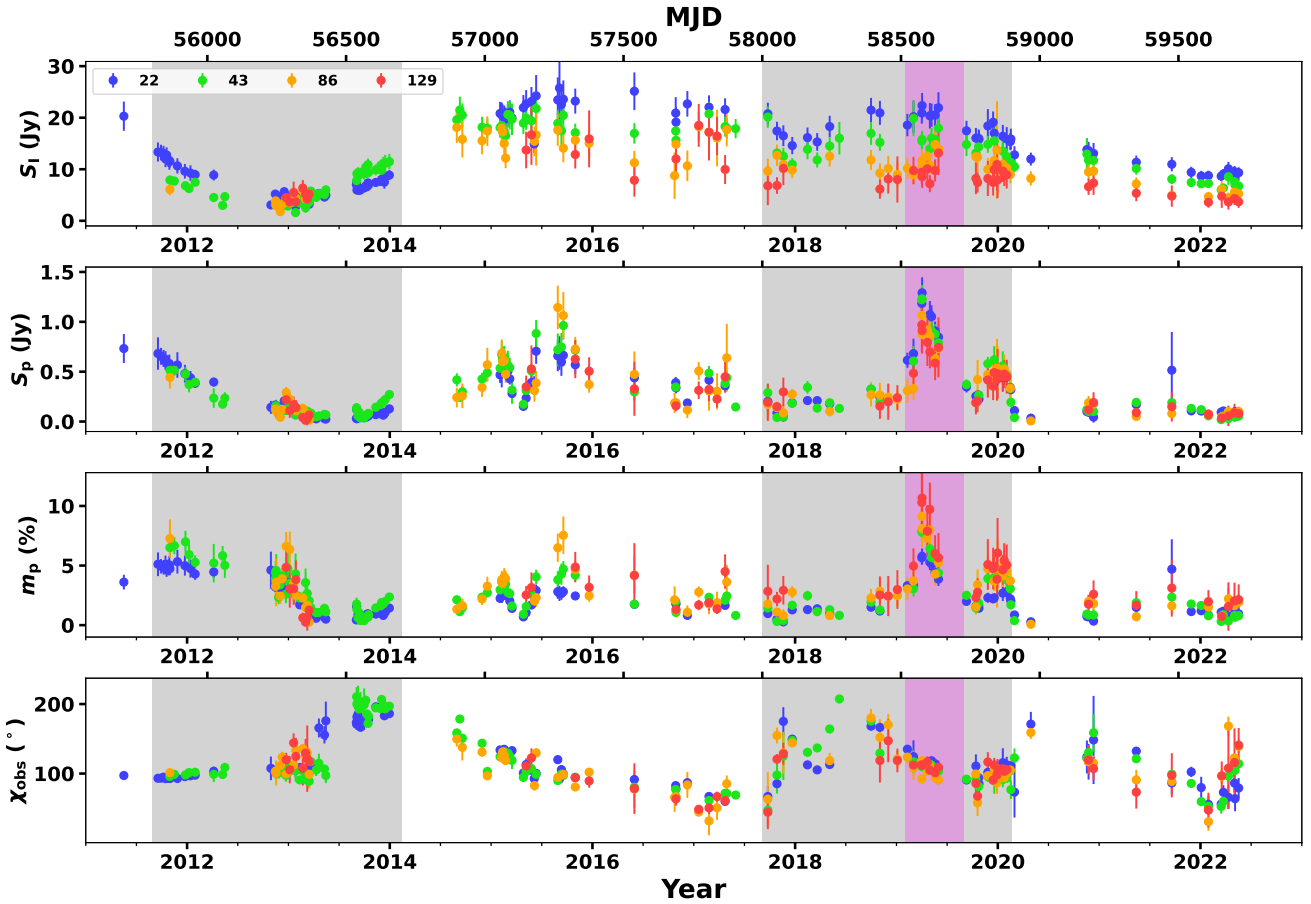


**Fig. 1.** Results of the KVN observations at 22 (blue), 43 (green), 86 (orange), and 129 GHz (red). Each panel shows the total flux density, linearly polarized flux density, polarization degree, and polarization angle (from top to bottom). The two time periods that we focus on in this work are shown in the gray shaded regions and discussed in Section 3.1. The magenta shaded area indicates a flaring period in polarized emission.

we applied an additional 10%, 10%, 15%, and 20% of uncertainties at 22, 43, 86, and 129 GHz, respectively<sup>5</sup>.

For this study, we mainly focused on two periods, around MJD 55800–56700 and MJD 58000–58900. At the beginning of the first period, 3C 454.3 exhibits a global decrease in its flux densities, while both  $m_p$  and  $\chi_{\text{obs}}$  remain constant until 2013 ( $\sim 5\%$ ,  $\sim 100^\circ$ ). After that, as polarized emission approaches its minimum state around MJD 56400,  $\chi_{\text{obs}}$  rotates to  $\sim 210^\circ$ , and  $S_I$  starts increasing at the same time. To investigate the jet evolution in the polarized emission during this period, we employed the VLBA 43 GHz maps and found different aspects between the core and Region C, as shown in Figure 2: the core becomes brighter, while Region C is fading out. When Region C dominates the polarized emission, it exhibits  $\chi_{\text{obs}} \approx 90^\circ$ . However, when the core dominates the emission,  $\chi_{\text{obs}}$  of the core appears  $\sim 30^\circ$  (i.e., nearly matching  $210^\circ$  in Figure 1). This suggests that the evolution in  $S_I$  and  $S_p$ , and the rotation in  $\chi_{\text{obs}}$  to  $\sim 210^\circ$  in the KVN data around MJD 56400 is the cause of the different evolution of the core and Region C.

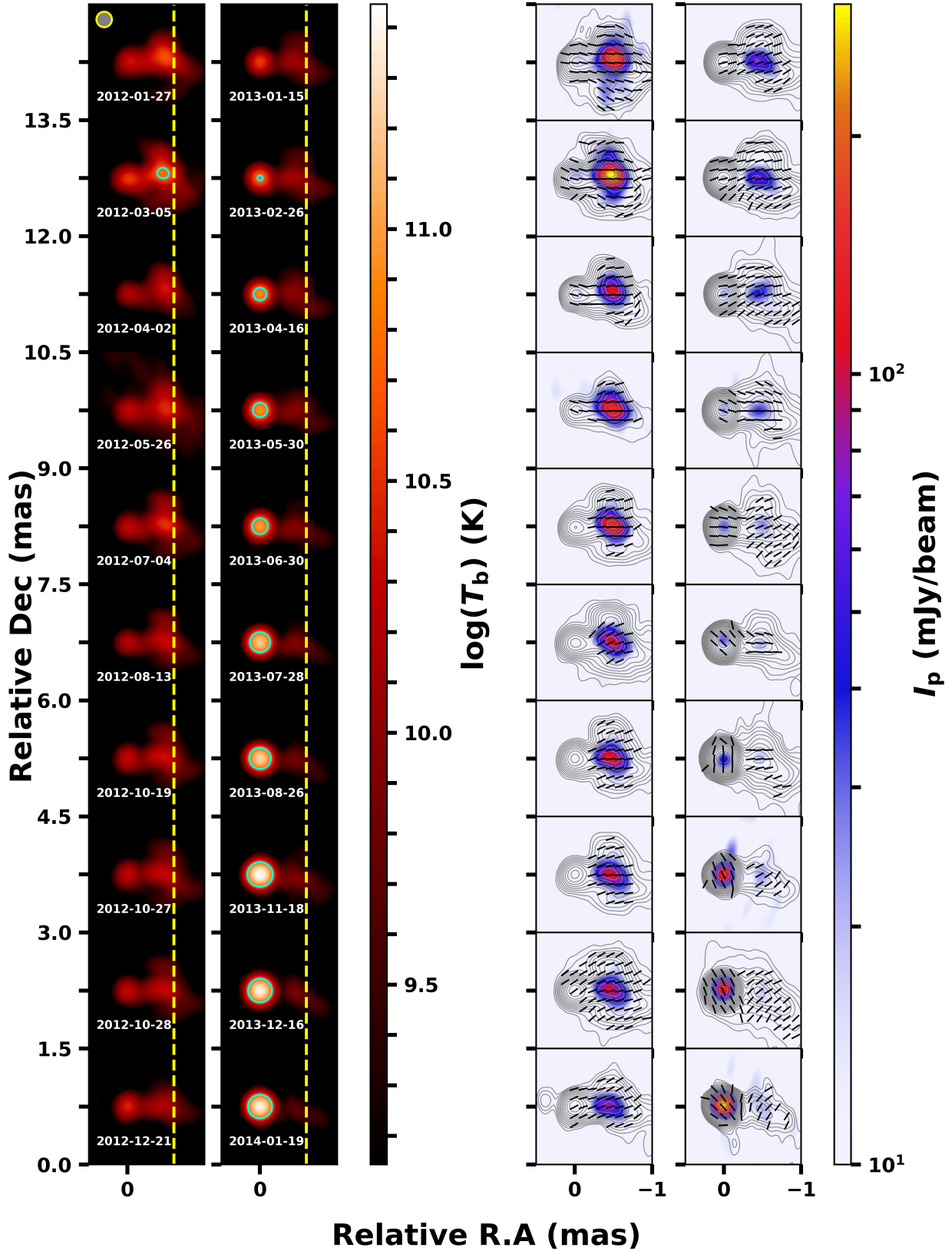
In late 2018 (i.e., second period, around MJD 58400), the angle rotates from  $\sim 150^\circ$  to  $\sim 100^\circ$  at 22, 43, and 86 GHz. At 129 GHz,  $\chi_{\text{obs}}$  at the beginning point deviates from  $150^\circ$ , but the uncertainty is quite large ( $118:8 \pm 20:9$ ). This rotation accompanies an increase in  $S_p$ , for example, at 129 GHz, by factors

of  $\geq 8$ , indicating a polarization flare. The estimated  $m_p$  reaches the maximum at all frequencies (e.g.,  $\sim 10\%$  at 129 GHz, as listed in Table B.1). We note that the increases in  $S_p$  and  $m_p$  were observed at all four frequencies, and  $m_p$  is clearly larger at higher frequencies around the peak of the flare. The chromatic evolution in  $m_p$  is possibly related to a physical condition, for example, a shocked region (see Section 4.4.3, and see also Tavecchio et al. 2018). In addition, the overall trend in variation among polarimetric measurements at all frequencies is comparable. This implies that the flaring event and its polarization variations at 22–129 GHz originated from a common emitting region in the relativistic jet.

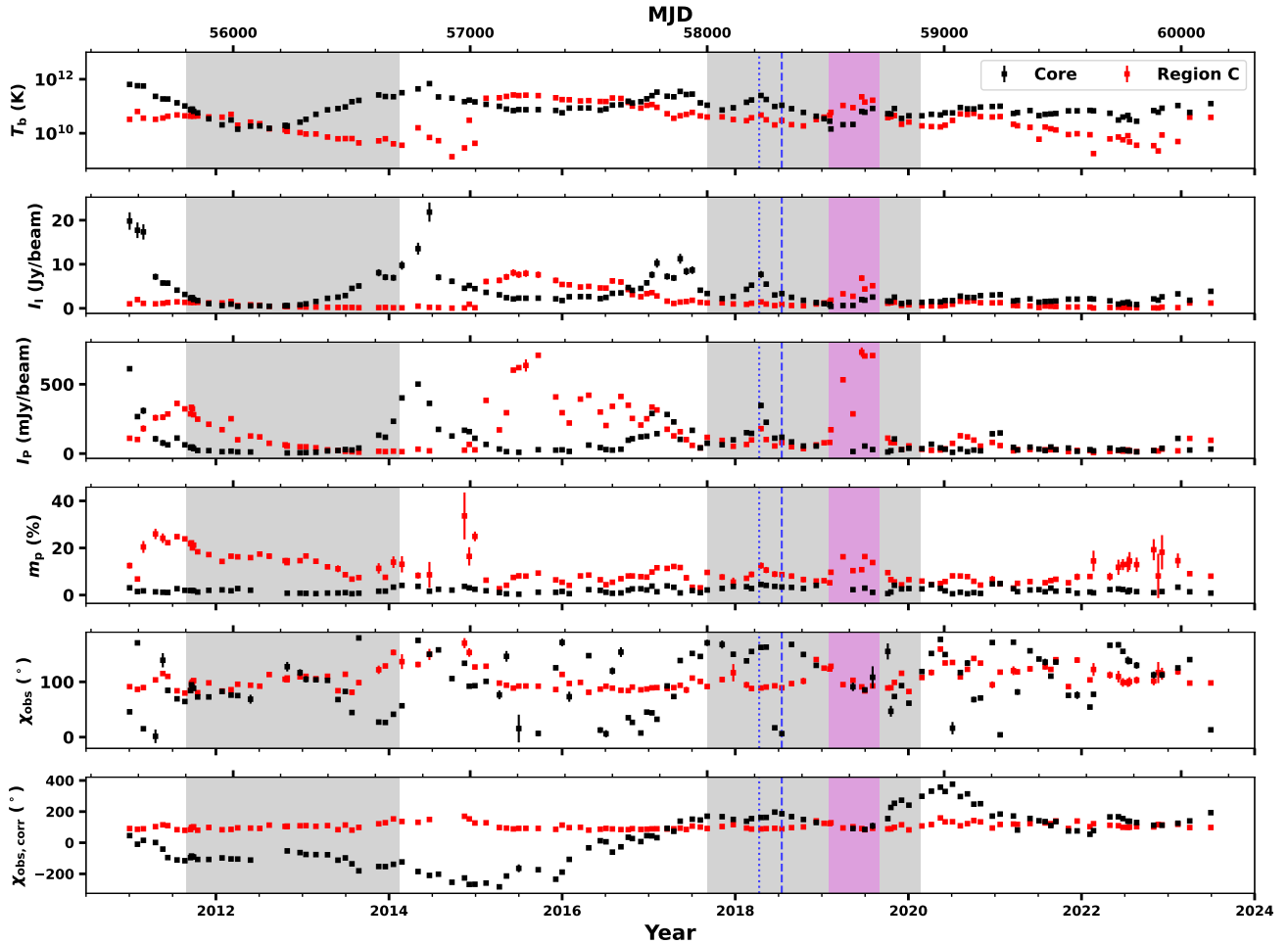
To investigate the resolved (high spatial resolution) polarization characteristics in the jet, the 43 GHz VLBA data was employed. The parameters ( $I_I$ ,  $I_p$ ,  $m_p$ , and  $\chi_{\text{obs}}$ ) were first computed for each pixel in the CLEAN map, and were then averaged over the pixels associated with each model component. The pixels were chosen from a box area with dimensions matched to the full width at half maximum of the corresponding Gaussian components. The corresponding errors were estimated following Hovatta et al. (2012). The obtained values from the CLEAN flux are consistent with the KVN 43 GHz single-dish data, especially in polarized emission as described in Appendix A.

Figure 3 shows the light curves of the core (black dots) and Region C (red dots). In general, the core displays higher  $I_I$  than Region C, while they alternate in dominance in  $I_p$ . Several peaks are clearly identified in both  $I_I$  and  $I_p$ .

<sup>5</sup> Lee et al. (2016) used 10%–30% of uncertainties in amplitude calibration. However, note that these are from VLBI observations, not single-dish observations.



**Fig. 2.** Left: 43 GHz VLBA images in terms of the brightness temperature  $T_b$  in the source rest frame. The right ascension of the radio core is fixed to 0. The cyan contours indicate where  $T_b = T_{\text{eq}} \approx 5 \times 10^{10}$  K. The yellow dashed lines present the location 0.6 mas from the core, a typical projected distance of Region C (0.45–0.7 mas; Weaver et al. 2022). Right: contours obtained from Stokes  $I$  images, starting from  $3\sigma_{\text{rms}}$  level, where  $\sigma_{\text{rms}}$  represents the r.m.s noise level in a residual map. The color maps show linear polarization intensity. All the images are convolved with a beam size of  $0.2 \times 0.2 \text{ mas}^2$ . The black bars indicate the observed polarization angle on the images where the S/N of the polarized emission is higher than 3.



**Fig. 3.** Estimated values of the regions related to the core and Region C at 43 GHz. Each value was obtained by computing the corresponding pixels. The first four panels (from top to bottom) indicate brightness temperature, total intensity, linearly polarized intensity, and polarization degree. The last two panels are polarization angles, but the one in the bottom panel was obtained after resolving the  $n\pi$ -ambiguity following the method in [Blinov et al. \(2016\)](#). The blue dotted and dashed lines show the ejection and segmentation time of knot B19 ([Weaver et al. 2022](#)).

Although, in general, the core presents relatively low polarization degrees ( $\lesssim 5\%$ , and mean value of  $\bar{m}_{p,\text{core}} \approx 2\%$ ), the  $\chi_{\text{obs}}$  of the core suggests rapid variation with  $180^\circ$  ambiguity to adjacent data points (i.e., in time). After resolving the continuous variation described in Section 3.1, we obtained a swing (approximately from  $-200^\circ$  to  $+400^\circ$ ) of  $\chi_{\text{obs}}$  from the core region on a long timescale.

Regarding Region C, the overall polarization degree  $m_p$  is higher than at the core, with the maximum value reaching  $\sim 20\%$  (and mean value of  $\bar{m}_{p,C} \approx 10\%$ ). The large uncertainties on  $m_p$  arise when the signal-to-noise ratio of Region C is low. Interestingly, the  $\chi_{\text{obs}}$  of this region is aligned to be  $\sim 100^\circ$  in a high-polarization state (e.g.,  $\geq 200$  mJy/beam) and deviates from that in low-polarization (e.g.,  $< 200$  mJy/beam) periods. In addition, several clear peaks in the polarized emission of Region C seem to have appeared after the flaring activities in the core. Given that Region C is the downstream region beyond the core, it is plausible to interpret that a moving knot induces activity when the knot arrives at Region C. [Jeong et al. \(2023\)](#) suggested that the  $\gamma$ -ray flare in August 2015 (about MJD 57250) is attributed to knot K14 (B12 knot defined in [Weaver et al. 2022](#)) when it arrived at Region C.

Correlations between the polarimetric measurements obtained from the KVN single-dish and the VLBA were investi-

gated, as shown in Figure 4:  $S_I/\chi_{\text{obs}} - S_p$  and  $I_I/\chi_{\text{obs}} - I_p$  (left) and  $m_p - \chi_{\text{obs}}$  (right).  $\chi_{\text{obs}}$  measured from the KVN were distributed with respect to  $\sim 100^\circ$  at all four frequencies when  $S_p$  was bright. Similar behavior was also found in Region C. The right panel also confirms this behavior of  $\chi_{\text{obs}}$ . These data indicate that a physical process increasing the polarized emission in Region C causes the observed relations.

### 3.2. Polarization angle and rotation measure

In this section, we present the results of RM using the KVN single-dish data. RM is a measurement that shows the Faraday screening effect of a foreground medium. As noted in Equation (1) ( $\text{RM} \propto \int n_e B_{\parallel} dl$ ), high RM indicates high  $n_e$ , strong  $B_{\parallel}$ , or both. Figure 5a presents the RMs obtained from a linear model fitting. The RMs are shown in log scale to illustrate the variation in magnitude, while the RM signs are described by red dots for a positive RM (i.e., parallel magnetic field toward us) and blue dots for a negative RM (i.e., magnetic field in the opposite direction). The number of frequencies in the linear fitting is described by filled and open circles, respectively.

We found that the order of RM values obtained from the linear fitting lie in a level of  $\sim 10^3$  rad  $\text{m}^{-2}$  and the mean value is approximately  $(-0.1 \pm 2.7) \times 10^2$  rad  $\text{m}^{-2}$ . Several sign flips

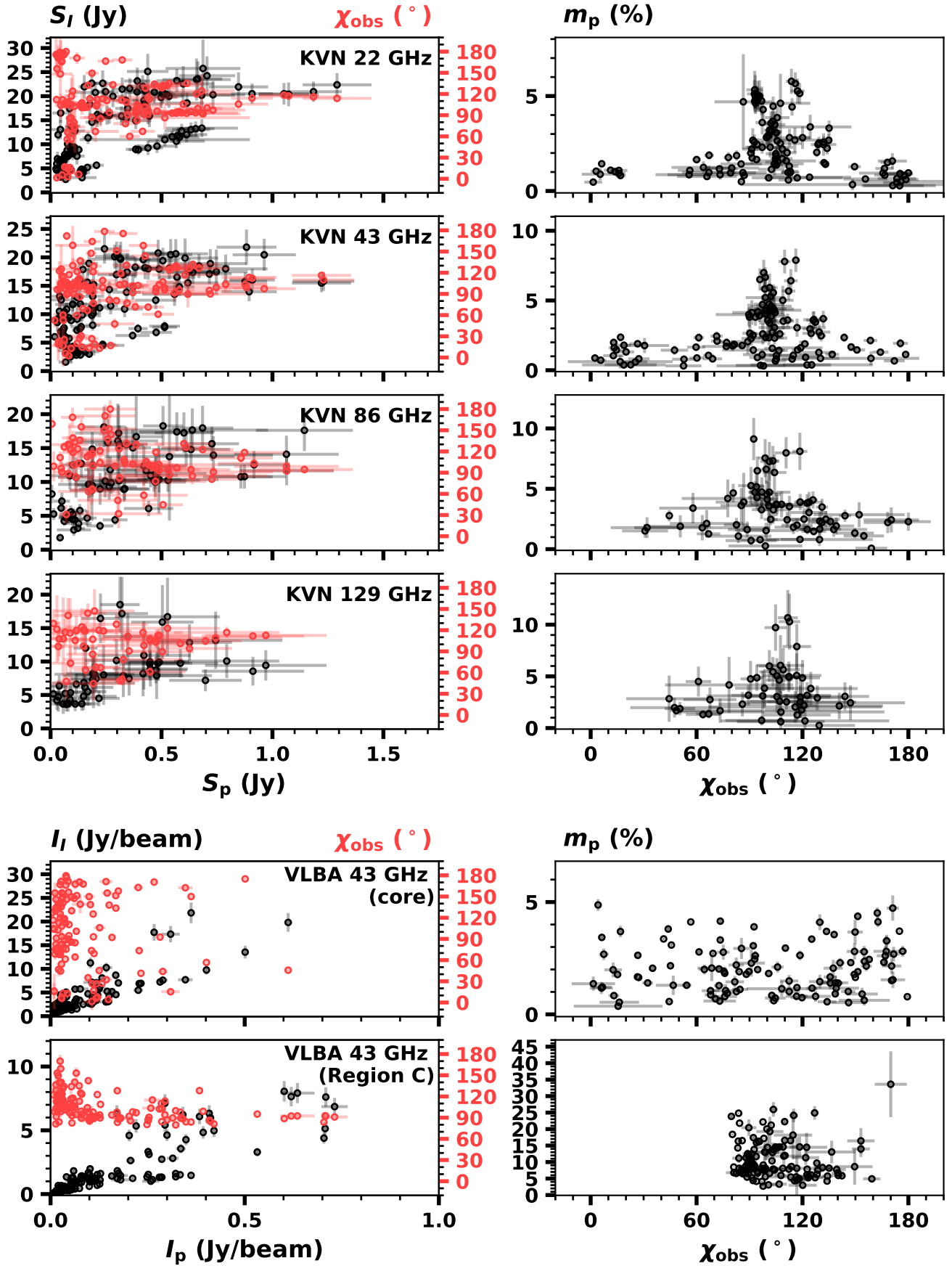
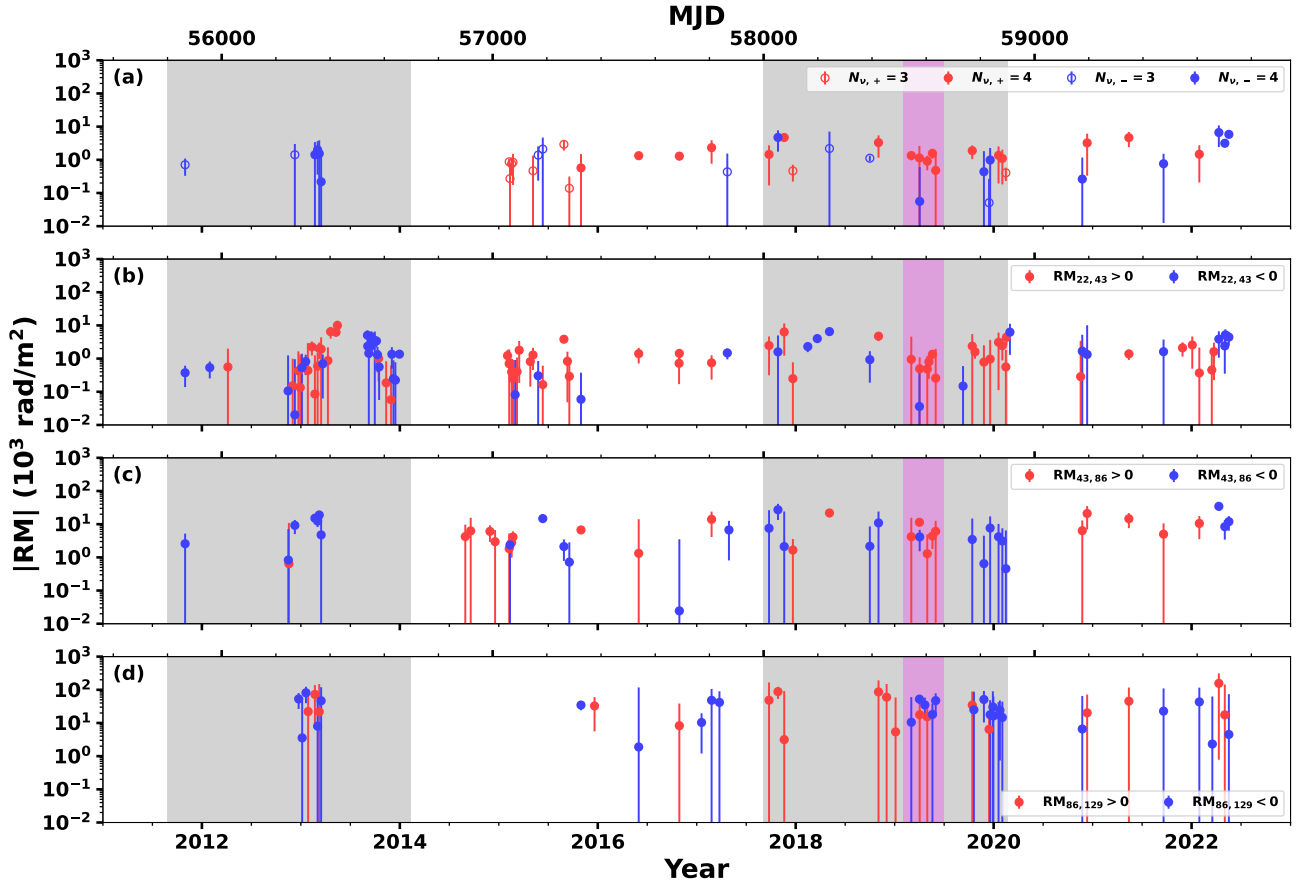


Fig. 4. Left: dependence of total emission (black symbols) and  $\chi_{obs}$  (red symbols) on polarized emission for the KVN data at different frequencies (first four panels) and the two different jet regions from the VLBA 43 GHz, the core and Region C (last two panels). Right: dependence of  $m_p$  on  $\chi_{obs}$ .



**Fig. 5.** RMs in the first panel (top) were obtained via linear fit ( $\chi = \chi_0 + \text{RM} \lambda^2$ ) if more than two data points were available. There are several large uncertainties ( $\sigma_{\text{RM}} \gtrsim |\text{RM}|$ ) attributed mainly to a significant deviation in  $\chi_{\text{obs}}$  to a linear relation. From the second to the last panels, RMs were calculated in pairs of 22–43 GHz (second), 43–86 GHz (third), and 86–129 GHz (bottom). RM signs are shown in color: blue and red for negative and positive signs, respectively. The filled and open circles in the first panel indicate the number of frequencies used in the fitting, four and three data points, respectively. Each shaded area is the same as in Figure 1.

appear, but they are not significant, given their uncertainty ranges. In a previous polarization monitoring study, the averaged RM of 3C 454.3 was reported to be  $(-2 \pm 52) \times 10^3 \text{ rad m}^{-2}$  at 86–229 GHz (Agudo et al. 2018b). Similarly, the absolute values in RM ( $|\text{RM}|$ ) suggest a variability in  $|\text{RM}|$  as well. In addition, in the fourth column in Figure B.1<sup>6</sup>, multiple epochs show  $\chi_{\text{obs}}$  values with large offsets from a single RM fit.

In order to focus on the epochs during which a single component dominates the polarized emission, the VLBA data was employed. For this work we studied the periods when Region C dominates the polarized emission. Based on  $m_p$  obtained from the KVN and 43 GHz VLBA images (Figure C.1), several epochs were selected as C-dominating periods: from February 2019 to June 2019. During these periods,  $m_p$  is high with chromatic behavior in frequency, indicating partially ordered magnetic field lines (see Figure B.1). In particular, we note that the amount of increased  $S_p$  is consistent at all frequencies and is remarkable compared to the pre-flare state. These results tentatively suggest that the polarimetric variations are mainly related to the evolution of Region C. The obtained  $\chi_{\text{obs}}$  at all frequencies are aligned near  $100^\circ$ , but it does not follow a simple linear relation with  $\lambda^2$ .

<sup>6</sup> Appendix B Figures are available on <https://zenodo.org/records/14967589>

## 4. Discussion

### 4.1. Total and polarized brightness evolution

Figure 1 shows the time variation in flux densities ( $S_I$  and  $S_p$ ), polarization degree ( $m_p$ ), and polarization angle ( $\chi_{\text{obs}}$ ) obtained from the KVN multifrequency single-dish observations. In this section we discuss the variations in two periods, MJD 55800–56700 and MJD 58000–58900 (shaded in gray).

In the period of MJD 55800–56100, both  $S_I$  and  $S_p$  decrease by a factor of about 0.6, while  $\chi_{\text{obs}}$  remains nearly constant (i.e.,  $\sim 100^\circ$ ) at 22 and 43 GHz. However, starting around MJD 56300, the light curves display different evolutions between total and polarized emission with rotation in  $\chi_{\text{obs}}$  from  $\sim 100^\circ$  to  $\sim 200^\circ$ : an increase in total flux density with a decrease in polarized flux density. The different evolutions are unlikely to originate from a single synchrotron emission region. If there were two or more emitting regions observed in a single-dish beam, the different evolutions in  $S_I$  and  $S_p$  can be explained; for example, one region dominant in polarized emission has diminished (decreasing  $S_p$ ), and then the other weakly polarized and fainter one becomes brighter and dominates the overall emission. It seems that two main regions dominate the overall emission in 3C 454.3 around this period: the core and the quasi-stationary Region C. As shown in Figure 3, while the core was bright in total intensity, the polarized intensity was predominant in Region C at the beginning of the first period. After that, Region C decayed in



polarized emission with a nearly constant  $\chi_{\text{obs}}$  while the core started increasing its brightness around MJD 56300.

In the beginning of the second period (MJD 58000–58900), while the source is bright in  $S_I$  it is not in  $S_p$  (Figure 1). However, starting from MJD 58400, both total and polarized emission increase at all the KVN frequencies, reaching  $S_p \sim 1000$  mJy and  $m_p \sim 10\%$  in April 2019. The obtained  $m_p$  exhibits chromatic behavior during the increasing stage. The amount of increase in polarized emission is similar among the frequencies. Unlike the behavior presented in the first period, the increase in both total and polarized emission may indicate a single highly polarized synchrotron emitting region leading the polarization evolution. In addition, we found that such activity also appears in Region C with  $I_p > 500$  mJy/beam, as shown in Figure 3; thus, in polarized emission, Region C was dominant and the core was quiet. Combining these results, we conclude that Region C is the origin of the polarization flare in 2019 at frequencies between 22 and 129 GHz.

#### 4.2. The origin of variation in polarization angle

In this study, we applied the methodology introduced in Blinov et al. (2016) for resolving  $n\pi$ -ambiguity in time as described in Section 3.1. As a cross-check, we also determined that the  $\chi_{\text{obs}}$  obtained from the VLBA data agree closely with that of the KVN at 43 GHz after resolving the ambiguity (Figure A.1).

The resultant angles obtained from the KVN show several variations (Figure 1). Even with these variations the polarimetric relations of  $\chi_{\text{obs}}$  reveal angles aligned to  $\sim 100^\circ$  when strongly polarized at all frequencies (Figure 4). This behavior is attributed to Region C, as described in Section 3.1, indicating that, in general, polarized emission is dominated by Region C when the source is strongly polarized.

Based on the VLBA 43 GHz data, we separately investigated the  $\chi_{\text{obs}}$  of the core and Region C using the corresponding pixels where each region is located, as shown in Figure 3. Interestingly, the core seems to suggest a long-term variation in  $\chi_{\text{obs}}$  after resolving a time- $n\pi$ -ambiguity. Possible explanations for this long-term variation are (i) helical magnetic field geometry with a bending within the core (for this case, one may find in Myserlis et al. 2018), (ii) rotation or  $\sim 90^\circ$  of flip in  $\chi_{\text{obs}}$  by an opacity effect (Lobanov 1998; Gabuzda & Gómez 2001; Porth et al. 2011; Chamani et al. 2023), or (iii) a stochastic random walk process (Blinov et al. 2015; Kiehlmann et al. 2017). Alternatively, it is also possible that the variation in  $\chi_{\text{obs}}$  is a biased result due to a relatively large cadence (about one month). Since the method we applied assumes no significant jump in  $\chi_{\text{obs}}$  ( $>90^\circ$ ) between the adjacent epochs, the related information may be biased if the intrinsic angle rotates faster than the observed cadence. For example, a rapid variation (e.g., spanning a few hours to a few days) in  $\chi_{\text{obs}}$  can occur via magnetic reconnection (Zhang et al. 2018, 2020). Possibly, high-cadence and long-term VLBI observations in the future would reveal whether this long-term variation is intrinsic or not.

Meanwhile, Region C suggests a specific angle, mostly between  $90^\circ$  and  $120^\circ$ . Among the observations collected in this study, one of the periods worth noting is around April 2019, showing a prominent polarization flaring activity in Region C, as identified in Section 4.1 (see also Figure 3). As the flare grows from the beginning ( $\sim$ MJD 58400), the  $\chi_{\text{obs}}$  values at all frequencies rotate into a direction parallel with the jet axis ( $\sim -80^\circ$ , Weaver et al. 2022). This rotation in  $\chi_{\text{obs}}$  with increased flux density implies a physical process in Region C. A polariza-

tion angle parallel to the jet axis is feasible through a dominant toroidal magnetic field component in the jet.

#### 4.3. Faraday rotation measure in arcsecond scales

The polarimetric measurements ( $\chi_{\text{obs}}$  and RM) used in Figure B.1 are listed in Tables B.1 and B.2. Figures 5b–d and B.2 show  $|RM|$  obtained from the KVN in the frequency domain. As presented, RM shows a large mean of  $|RM| \gtrsim 10^3$  rad/m<sup>2</sup> as well as a variability not only in its magnitude, but also in its sign. These imply that an external medium is unlikely to be the main reason for the Faraday screening medium if present.

The calculated mean of  $|RM|$  in the available periods are  $2.9 \pm 0.2$ ,  $7.4 \pm 1.3$ , and  $32.6 \pm 11.6$  in units of  $10^3$  rad m<sup>-2</sup> at 22–43, 43–86, and 86–129 GHz pairs, respectively (see Section 3.2). Although it seems to suggest frequency-dependent  $|RM|$ , one needs to be careful in interpreting frequency dependence in  $|RM|$  as systematic effects may affect  $|RM|$ .

There are several origins of the time variability and frequency dependence of RM. For example, the variability can be attributed to the dynamics in the jet, such as turbulence or helical magnetic field lines, since it depends on the direction of magnetic field lines toward us. Zamaninasab et al. (2013) found evidence of a large-scale helical field structure in the jet of 3C 454.3 through multifrequency VLBI observations.

Alternatively, we could not rule out the possible beam convolution effect (i.e., beam depolarization) on RM variability at other frequencies, although we have identified consistent polarized emission of the source on arcsecond and milliarcsecond scales at 43 GHz. The source has a complex jet structure (on milliarcsecond scale) not only in total emission, but also in polarized emission, as shown in Figures 2 and C.1. The complex jet structure with large beam sizes in the KVN single-dish observations possibly results in rotation in  $\chi_{\text{obs}}$  through a beam convolution effect attributed to  $|RM|$  variation. For this reason, we selected a few epochs (from February 2019 to June 2019) in which Region C dominates the polarized emission of 3C 454.3 at 43 GHz and found the frequency dependence in  $|RM|$  in those epochs.

To understand the frequency-dependency  $|RM|$  of 3C 454.3 shown in this work in more detail, we consider the opacity effect to  $\chi_{\text{obs}}$ . As the synchrotron emission becomes optically thick at low frequency, it is possible that the opacity effect rotates  $\chi_{\text{obs}}$  by about  $90^\circ$  (Gabuzda & Gómez 2001; Porth et al. 2011). Alternatively, the frequency dependence can be related to the core-shift effect (Lobanov 1998). As described in Jorstad et al. (2007), if the Faraday screening medium is very close to the jet, such as a sheath layer, frequency-dependent  $|RM|$  can be obtained.

However, the downstream jet, Region C, is expected to be optically thin in the KVN observing frequency range, restricting us from considering the opacity effect as the origin of the frequency-dependent  $|RM|$ . In addition, we cannot be confident if the polarized emission from the core is faint at higher frequencies (86 and 129 GHz). If the core has prominent polarized emission compared to Region C at these frequencies, then  $\chi_{\text{obs}}$  may be affected by this.

We consider that the frequency-dependent  $|RM|$  shown in this work is most likely attributed to complex and unresolved polarized emission regions within 1 mas (i.e., the case of beam convolution) rather than an external Faraday screening medium. Traianou et al. (2024) studied spatially resolved polarized emission in 3C 454.3 using VLBI observations at 43 and 86 GHz. As shown in their work, the core and Region C have different spectral indices at 43 and 86 GHz: flat and thin spectra for the core and Region C, respectively, resulting in different morphologies

in total intensity and polarization at 43 and 86 GHz (i.e., showing complex structure). Therefore, high-resolution multifrequency VLBI observations in full-polarization mode would be required to perform a more detailed analysis of RM variability in the jet.

#### 4.4. Origins of a polarization flare in Region C

In Section 4.1, we identify that the flaring region is related to Region C based on a consistent evolution in flux density across the KVN frequencies, and based on the VLBA 43 GHz maps. In addition,  $\chi_{\text{obs}}$  rotates from  $\sim 150^\circ$  to  $\sim 100^\circ$  during the flare. Since the core region was faint with several non-detections in polarization during this period, we interpret that the increasing  $|\text{RM}|$  with frequency and other polarimetric properties are related to a physical process in Region C. To understand this, we consider three cases: (i) jet–medium interaction, (ii) magnetic reconnection, and (iii) shock–shock interaction. Finally, we investigate how the Doppler boosting effect via a change in viewing angle can describe the observed brightness increase.

##### 4.4.1. Jet–medium interaction

For the first scenario, a jet interacting with an ambient medium may result in a high RM. The broad-line region (BLR) and the narrow-line region (NLR) are the possible candidates for this medium. In addition, the jet can be bent toward us by the collision, leading to an increase in the Doppler factor, and thus the brightness as well. However, we note the de-projected location of Region C is  $d_C \approx 200$  pc from the core by adopting a mean viewing angle  $\theta_{v,\text{mean}} \approx 1^\circ 4$  (see Table 12 in Weaver et al. 2022), and its projected distance from the core of  $\sim 0.6$  mas. The distance of BLR in 3C 454.3 is  $d_{\text{BLR}} \approx 0.2$  pc (Bonnoli et al. 2011; Costamante et al. 2018), which was estimated using the size–luminosity relation. Moreover, based on the activity in optical line emission, Amaya-Almazán et al. (2021) interpreted that the increase in continuum emission during a flaring period (FP2, approximately 2014–2017), in which Region C brightened, was not strongly related to the BLR. Therefore, we exclude the BLR from the dense cloud candidate. If the medium corresponds to the NLR at parsec to kiloparsec scales, we expect a stable  $n_e$ ,  $B_{\parallel}$ , and path length. In this case, the estimated RM magnitude and its sign would not vary significantly either in time or frequency. However, we would expect constant RM across the observing frequencies and time if the Faraday screening medium were related to the NLR. Therefore, we suggest that the NLR is also less likely to cause the flare with variation in RM via jet–medium collision.

##### 4.4.2. Magnetic reconnection

Alternatively, magnetic reconnection, a physical process of rejoining two oppositely aligned magnetic field lines, can introduce increased  $n_e$ , magnetic field strength, and the acceleration of plasmoids in the jet region (Zhang et al. 2018; Nathanail et al. 2020; Sironi et al. 2021). Given the magnetic energy density dominance in Region C, as reported in Jeong et al. (2023), this region is suitable for magnetic reconnection. The magnetic dominance can also be supported by having a brightness temperature ( $T_b$ ) lower than the equipartition condition ( $T_{\text{eq}} \approx 5 \times 10^{10}$  K, Readhead 1994). Figure C.1 shows the  $T_b$  estimated in the source rest frame. The obtained  $T_b$  of Region C was lower than  $T_{\text{eq}}$  before a moving knot arrived in Region C, indicating a possible magnetic dominance.

By using particle-in-cell (PIC) simulations, Petropoulou et al. (2016) studied the physics of plasmoids in a relativistic jet, which is formed by the fragmentation of reconnection current sheets (current sheets derived by magnetohydrodynamic instability), which is a region containing magnetic field lines and energetic particles. From the simulation they found that the highest emission is observed when a plasmoid leaves the current sheet layer. Zhang et al. (2020) investigated the signatures in the polarization of magnetic reconnection in blazars at multi-wavelengths. In their work, magnetic field lines are found to be disordered when a reconnection layer segments into several plasmoids. This results in a low  $m_p$  when the observed total emission peaks due to depolarization by the tangled magnetic field lines in a plasmoid. In our study, however, we obtained increasing  $m_p$  and  $S_p$  as  $S_I$  increases during the flare in 2019. Therefore, we consider that magnetic reconnection is less likely to govern the physics in Region C.

##### 4.4.3. Shock–shock interaction

In the last scenario,  $n_e$  and  $B_{\parallel}$  in a jet can also be increased via shock–shock interaction, leading to the compression of a jet region. Previous studies on 3C 454.3 at high resolution have identified a quasi-stationary behavior of Region C, although a marginal motion was observed at a distance range of 0.45–0.7 mas from the core (Jorstad et al. 2017; Weaver et al. 2022). The motion is possibly related to the intrinsic physics of Region C, but as suggested in Weaver et al. (2022), it also can be explained by the relative motion of the core produced by the core-shift effect. Liodakis et al. (2020) explained the spatial variation in Region C with the emergence of a new jet component from the core.

The possibility of Region C as a recollimation or standing shock has been discussed in previous studies (Gómez et al. 1999; Jeong et al. 2023; Traianou et al. 2024). If Region C is related to a shock, its interaction with an upstream shock moving downstream is considered a shock–shock interaction. In this case, the intrinsic polarization angle of the shocked region will be parallel with the jet axis due to the compression of magnetic field components perpendicular to the jet axis (Marscher 2014) for the case of conical shock or self-generated magnetic field lines that are predominantly aligned in a direction parallel to the shock front (Tavecchio et al. 2018).

Moreover, in the shock–shock interaction scenario, a chromatic behavior in  $m_p$  with observing frequency is expected based on the energy-stratified model (Tavecchio et al. 2018, 2020; Liodakis et al. 2022). In the region where the jet is most compressed, such as the Mach disk or shock front, the magnetic field lines are expected to be ordered, and thus a high  $m_p$  is observed. Beyond the region (downstream of the jet), the jet expands, and the magnetic field lines are relatively disordered as it flows downstream, leading to low  $m_p$ . Since high-energy electrons undergo a stronger radiative cooling process than low-energy electrons, the dominant emission region at higher frequencies is closer to the compressing region than at lower frequencies. As shown in Figure B.1 and Table B.1,  $m_p$  is as high as  $\sim 10\%$  at high frequencies, but is rather low ( $\sim 5\%$ ) at 22 and 43 GHz during the flare. If the extended jet (e.g.,  $\gtrsim 1$  mas; see also Figure C.1) of 3C 454.3 is highly polarized,  $m_p$  can be depolarized via the beam depolarization effect, especially at low frequencies. However,  $S_p$  and  $m_p$  are comparable at scales between milliarcsecond and arcsecond, as shown in Figure A.1, and thus we expect the extended jet to have a negligible effect on the polarized emission at frequencies higher than 43 GHz.

Furthermore, we also expect a negligible depolarization effect by turbulent magnetic fields if Region C is related to the shock interaction showing well-ordered magnetic field lines.

It is also possible that Region C is related to an oblique shock rather than a simple recollimation or standing shock. In the case of an oblique shock, the jet direction potentially varies by jet instabilities or jet bending. In particular, the jet of 3C 454.3 has a very narrow viewing angle ( $\theta_v$ ), so its brightness is sensitive to the jet flow direction via the Doppler boosting effect, as discussed in a previous study (Traianou et al. 2024). Therefore, it is essential to examine if the pure jet bending can explain the observed brightness increase during the polarization flare.

#### 4.4.4. Changes in viewing angle

As blazar jets generally have  $\theta_v$  smaller than  $10^\circ$ , a change in  $\theta_v$  can induce strong variability. Traianou et al. (2024) suggested Region C as a bent jet region to explain the disappearance of a moving knot and brightness increase. In a similar way, we investigated the variation in Doppler factor  $\delta$  to determine whether the increased  $S_I$  and  $S_p$  during the flare were strongly attributable to the change in  $\theta_v$ . As shown in Figure C.1, a plasma blob having  $T_b \gtrsim T_{eq}$  was identified and ejected downstream from the core to Region C. Given its ejection time, the plasma blob is likely related to the knot B19 defined in Weaver et al. (2022). As the blob approaches Region C,  $T_b$  increases with a peak value of  $\sim 2.6 \times 10^{11}$  K. Compared to the minimum peak value of the blob ( $T_{b,min} \approx 7.3 \times 10^{10}$  K) during its ejecting period, the brightness increased by a factor of more than three. After crossing Region C, the blob seems to move further downstream with reduced  $T_b$ . We note that  $T_b$  is computed in the source rest frame, so the only factors that can change  $T_b$  are particle acceleration and/or energy loss or a change in viewing angle that affects  $\delta$ .

To evaluate the Doppler boosting effect by viewing angle, we adopt the apparent speed of knot B19 and the mean viewing angle of 3C 454.3 as  $\beta_{app} = 18 \pm 1.8$  and  $\theta_{v,mean} = 1^\circ 4 \pm 0^\circ 4$ , respectively (see Tables 8 and 12 in Weaver et al. 2022). At this angle, we obtain the bulk Lorentz factor of B19 as  $\Gamma \approx 21.7 \pm 1.4$ . By assuming a constant  $\Gamma$  of the knot during its journey, we find the ratio of the Doppler factors at viewing angles of  $\theta_v = 1^\circ 4 \pm 0^\circ 4$  and  $0^\circ$  to be  $\sim 1.28 \pm 0.16$ . Based on the observed ratio of  $\delta$  higher than three, we conclude that by itself a change in  $\theta_v$  is insufficient to describe the increased  $T_b$ , implying an additional source intrinsic process, such as particle acceleration.

Although the observational results favor an additional particle acceleration in Region C by a shock–shock interaction, the lack of emission beyond the region leaves an open question. If the region has a very steep optically thin spectrum, for example, due to a strong cooling process, this can explain the absence of emission. A high-resolution analysis at multifrequency, including low-frequency (e.g., 15 GHz), would be required to investigate spectral information beyond Region C.

## 5. Conclusions

In this work we studied the polarimetric variations of 3C 454.3 using decadal data (2011–2022) at millimeter wavelengths. We found several notable polarimetric features, especially in 2013–2014, and 2019. We summarize our results and conclusions as follows:

1. At all frequencies used in this work, relations between the polarimetric characteristics show a trend of  $\chi_{obs} \approx 100^\circ$  when the polarized emission is strong (Figure 4). By analyzing

the VLBA data, we found that Region C yields consistent results, indicating a prominent polarized jet region downstream of the radio core even at 129 GHz. While the  $\chi_{obs}$  of Region C does not change after resolving the  $n\pi$ -ambiguity in time (Blinov et al. 2016), the  $\chi_{obs}$  of the radio core exhibits a large long-term swing.

2. Around 2013–2014,  $\chi_{obs}$  rotated from  $\sim 100^\circ$  to  $\sim 200^\circ$  with decreasing  $S_p$  and prominent variations in  $|RM|$  at 22–43 GHz pair. From the VLBA 43 GHz data, we found that Region C dominated the polarized emission at milliarcsecond scale and then decayed in all emission ( $S_I$  and  $S_p$ ) during this period. At the same time, the core emission was enhanced. These imply that the rotation in  $\chi_{obs}$  and the  $|RM|$  variation did not originate from a common emitting region, but can be attributed to the co-evolution of Region C and the core.
3. A notable polarization flaring event in 2019 was captured in the KVN observations. Even though this activity increased the total emission slightly, a prominent evolution appeared in the polarized emission. During the flaring period, the  $\chi_{obs}$  at all the KVN observing frequencies rotated toward  $\sim 100^\circ$  with partially ordered magnetic field lines (e.g.,  $m_p \gtrsim 10\%$  at 129 GHz). By investigating high angular resolution maps from the VLBA at 43 GHz, we identified that the polarization flare occurred in Region C when a moving blob (possibly related to knot B19 in Weaver et al. 2022) arrived at Region C.
4. To describe the flare in Region C and to investigate which physical process is favorable for the flare, we considered several cases: (i) jet-cloud interaction via BLR or NLR is unlikely to cause the flare based on the de-projected distance of Region C, the lack of optical line emission (Amaya-Almazán et al. 2021), and variable RM; (ii) magnetic reconnection is excluded due to the opposite evolution in  $m_p$  between the PIC simulation (decreasing  $m_p$ , Zhang et al. 2020) and our observations (increasing  $m_p$ ) during the flare; (iii) shock–shock interaction can explain the overall observational results (chromatic  $m_p$ , concurrent rise in  $S_I$  and  $m_p$ , and  $\chi_{obs}$  parallel to the jet axis) (Marscher 2014; Tavecchio et al. 2018, 2020; Liodakis et al. 2020). Therefore, we suggest that a shock–shock interaction is the most likely mechanism for the flare in 2019.
5. We also investigated a possible beaming effect caused by a local bending of the jet for some reason. The mean  $\theta_v$  of 3C 454.3 was obtained as  $1^\circ 4 \pm 0^\circ 4$  by averaging those of several knots (Weaver et al. 2022). By adopting the apparent speed of knot B19 as  $\beta_{app} \approx 18 \pm 1.8$ , we obtained the resultant Doppler factor  $\delta \approx 33.9 \pm 4.4$  for the knot. In the assumption of constant  $\Gamma$  of the moving knot, the Doppler factor at  $\theta_v = 0^\circ$  was computed to be  $\delta_0 \approx 43.5 \pm 2.8$ . Therefore, the change in  $\theta_v$  toward us can increase  $\delta$  by  $1.28 \pm 0.16$ , and this is insufficient to explain the observed increased brightness of about 3.5 times. Provided with this and the favored physical model, we interpret that the shock–shock interaction may be responsible for the polarization flaring activity in Region C with additional particle acceleration.

## Data availability

The Appendix B figures are available on <https://zenodo.org/records/14967589>

*Acknowledgements.* We thank Thomas Krichbaum, Alan Marscher, and Svetlana Jorstad for reading the manuscript and helping us to improve it with

valuable comments. The KVN is a facility operated by the KASI (Korea Astronomy and Space Science Institute). The KVN observations and correlations are supported through high-speed network connections among the KVN sites provided by the KREONET (Korea Research Environment Open Network), which is managed and operated by KISTI (Korea Institute of Science and Technology Information). This work was supported by the National Research Foundation of Korea (NRF) grant funded by the Korea government (MIST) (2020R1A2C2009003, RS-2025-00562700). We also acknowledge financial support from the National Research Foundation of Korea (NRF) grant 2022R1F1A1075115. This study makes use of VLBA data from the VLBA-BU Blazar Monitoring Program (BEAM-ME and VLBA-BU-BLAZAR; <http://www.bu.edu/blazars/BEAM-ME.html>), funded by NASA through the Fermi Guest Investigator Program. The VLBA is an instrument of the National Radio Astronomy Observatory. The National Radio Astronomy Observatory is a facility of the National Science Foundation operated by Associated Universities, Inc. This work made use of Astropy: (<http://www.astropy.org>) a community-developed core Python package and an ecosystem of tools and resources for astronomy (Astropy Collaboration 2013, 2018, 2022).

## References

- Agudo, I., Thum, C., Wiesemeyer, H., et al. 2012, *A&A*, 541, A111  
 Agudo, I., Thum, C., Molina, S. N., et al. 2018a, *MNRAS*, 474, 1427  
 Agudo, I., Thum, C., Ramakrishnan, V., et al. 2018b, *MNRAS*, 473, 1850  
 Amaya-Almazán, R. A., Chavushyan, V., & Patiño-Álvarez, V. M. 2021, *ApJ*, 906, 5  
 Angelakis, E., Hovatta, T., Blinov, D., et al. 2016, *MNRAS*, 463, 3365  
 Astropy Collaboration (Robitaille, T. P., et al.) 2013, *A&A*, 558, A33  
 Astropy Collaboration (Price-Whelan, A. M., et al.) 2018, *AJ*, 156, 123  
 Astropy Collaboration (Price-Whelan, A. M., et al.) 2022, *ApJ*, 935, 167  
 Aumont, J., Conversi, L., Thum, C., et al. 2010, *A&A*, 514, A70  
 Blinov, D., & Pavlidou, V. 2019, *Galaxies*, 7, 46  
 Blinov, D., Pavlidou, V., Papadakis, I., et al. 2015, *MNRAS*, 453, 1669  
 Blinov, D., Pavlidou, V., Papadakis, I., et al. 2016, *MNRAS*, 462, 1775  
 Bonnoli, G., Ghisellini, G., Foschini, L., Tavecchio, F., & Ghirlanda, G. 2011, *MNRAS*, 410, 368  
 Burn, B. J. 1966, *MNRAS*, 133, 67  
 Buson, S. 2014, *The Astronomer's Telegram*, 6236, 1  
 Chamani, W., Savolainen, T., Ros, E., et al. 2023, *A&A*, 672, A130  
 Clark, B. G. 1980, *A&A*, 89, 377  
 Cornwell, T., Braun, R., & Briggs, D. S. 1999, in *Synthesis Imaging in Radio Astronomy II*, eds. G. B. Taylor, C. L. Carilli, & R. A. Perley, *ASP Conf. Ser.*, 180, 151  
 Costamante, L., Cutini, S., Tosti, G., Antolini, E., & Tramacere, A. 2018, *MNRAS*, 477, 4749  
 Dahal, S., Brewer, M. K., Akins, A. B., et al. 2023, *PSJ*, 4, 154  
 de Pater, I., Sault, R. J., Moeckel, C., et al. 2019, *AJ*, 158, 139  
 Di Gesu, L., Donnarumma, I., Tavecchio, F., et al. 2022, *ApJ*, 938, L7  
 Gabuzda, D. C., & Gómez, J. L. 2001, *MNRAS*, 320, L49  
 Gómez, J.-L., Marscher, A. P., & Alberdi, A. 1999, *ApJ*, 522, 74  
 Högbom, J. A. 1974, *A&AS*, 15, 417  
 Hovatta, T., Lister, M. L., Aller, M. F., et al. 2012, *AJ*, 144, 105  
 Hovatta, T., O'Sullivan, S., Martí-Vidal, I., Savolainen, T., & Tchekhovskoy, A. 2019, *A&A*, 623, A111  
 Hull, C. L. H., & Plambeck, R. L. 2015, *Journal of Astronomical Instrumentation*, 4, 1550005  
 Jeong, H.-W., Lee, S.-S., Cheong, W. Y., et al. 2023, *MNRAS*, 523, 5703  
 Jorstad, S. G., Marscher, A. P., Lister, M. L., et al. 2005, *AJ*, 130, 1418  
 Jorstad, S. G., Marscher, A. P., Stevens, J. A., et al. 2007, *AJ*, 134, 799  
 Jorstad, S. G., Marscher, A. P., Smith, P. S., et al. 2013, *ApJ*, 773, 147  
 Jorstad, S., Larionov, V., Mokrushina, A., Troitsky, I., & Morozova, D. 2015, *The Astronomer's Telegram*, 7942, 1  
 Jorstad, S. G., Marscher, A. P., Morozova, D. A., et al. 2017, *ApJ*, 846, 98  
 Kam, M., Trippe, S., Byun, D.-Y., et al. 2023, *Journal of Korean Astronomical Society*, 56, 1  
 Kang, S., Lee, S.-S., & Byun, D.-Y. 2015, *Journal of Korean Astronomical Society*, 48, 257  
 Kembell, A. J., Diamond, P. J., & Pauliny-Toth, I. I. K. 1996, *ApJ*, 464, L55  
 Kiehlmann, S., Savolainen, T., Jorstad, S. G., et al. 2016, *A&A*, 590, A10  
 Kiehlmann, S., Blinov, D., Pearson, T. J., & Liodakis, I. 2017, *MNRAS*, 472, 3589  
 Kim, D. E., Di Gesu, L., Liodakis, I., et al. 2024, *A&A*, 681, A12  
 Kuo, C. Y., Asada, K., Rao, R., et al. 2014, *ApJ*, 783, L33  
 Kutkin, A. M., Sokolovsky, K. V., Lisakov, M. M., et al. 2014, *MNRAS*, 437, 3396  
 Lee, S.-S., Wajima, K., Algaba, J.-C., et al. 2016, *ApJS*, 227, 8  
 Liodakis, I., Blinov, D., Jorstad, S. G., et al. 2020, *ApJ*, 902, 61  
 Liodakis, I., Marscher, A. P., Agudo, I., et al. 2022, *Nature*, 611, 677  
 Lister, M. L., Aller, M. F., Aller, H. D., et al. 2018, *ApJS*, 234, 12  
 Lister, M. L., Homan, D. C., Kellermann, K. I., et al. 2021, *ApJ*, 923, 30  
 Lobanov, A. P. 1998, *A&A*, 330, 79  
 Marinucci, A., Muleri, F., Dovciak, M., et al. 2022, *MNRAS*, 516, 5907  
 Marscher, A. P. 2014, *ApJ*, 780, 87  
 Martí-Vidal, I., Muller, S., Vlemmings, W., Horellou, C., & Aalto, S. 2015, *Science*, 348, 311  
 Middei, R., Liodakis, I., Perri, M., et al. 2023a, *ApJ*, 942, L10  
 Middei, R., Perri, M., Puccetti, S., et al. 2023b, *ApJ*, 953, L28  
 Mohan, P., Agarwal, A., Mangalam, A., et al. 2015, *MNRAS*, 452, 2004  
 Myserlis, I., Komossa, S., Angelakis, E., et al. 2018, *A&A*, 619, A88  
 Nagai, H., Nakanishi, K., Paladino, R., et al. 2016, *ApJ*, 824, 132  
 Nathanael, A., Fromm, C. M., Porth, O., et al. 2020, *MNRAS*, 495, 1549  
 Ojha, R. 2016, *The Astronomer's Telegram*, 9190, 1  
 Panebianco, G., Bulgarelli, A., Pittori, C., et al. 2022, *The Astronomer's Telegram*, 15782, 1  
 Park, J., Kam, M., Trippe, S., et al. 2018, *ApJ*, 860, 112  
 Peiron, A. L., Negro, M., Liodakis, I., et al. 2023, *ApJ*, 948, L25  
 Perley, R. A., & Butler, B. J. 2013, *ApJS*, 206, 16  
 Petropoulou, M., Giannios, D., & Sironi, L. 2016, *MNRAS*, 462, 3325  
 Planck Collaboration XXVI. 2016, *A&A*, 594, A26  
 Porth, O., Fendt, C., Meliani, Z., & Vaidya, B. 2011, *ApJ*, 737, 42  
 Pushkarev, A. B., Hovatta, T., Kovalev, Y. Y., et al. 2012, *A&A*, 545, A113  
 Pushkarev, A. B., Aller, H. D., Aller, M. F., et al. 2023, *MNRAS*, 520, 6053  
 Readhead, A. C. S. 1994, *ApJ*, 426, 51  
 Rybicki, G. B., & Lightman, A. P. 1979, *Radiative Processes in Astrophysics* (New York: Wiley)  
 Shepherd, M. C. 1997, in *Astronomical Data Analysis Software and Systems VI*, eds. G. Hunt, & H. Payn, *ASP Conf. Ser.*, 125, 77  
 Sironi, L., Rowan, M. E., & Narayan, R. 2021, *ApJ*, 907, L44  
 Sokoloff, D. D., Bykov, A. A., Shukurov, A., et al. 1998, *MNRAS*, 299, 189  
 Tavecchio, F., Landoni, M., Sironi, L., & Coppi, P. 2018, *MNRAS*, 480, 2872  
 Tavecchio, F., Landoni, M., Sironi, L., & Coppi, P. 2020, *MNRAS*, 498, 599  
 Traianou, E., Krichbaum, T. P., Gómez, J. L., et al. 2024, *A&A*, 682, A154  
 Trippe, S. 2014, *Journal of Korean Astronomical Society*, 47, 15  
 Weaver, Z. R., Jorstad, S. G., Marscher, A. P., et al. 2022, *ApJS*, 260, 12  
 Weiland, J. L., Odegard, N., Hill, R. S., et al. 2011, *ApJS*, 192, 19  
 Zamaninasab, M., Savolainen, T., Clausen-Brown, E., et al. 2013, *MNRAS*, 436, 3341  
 Zhang, H., Li, X., Guo, F., & Giannios, D. 2018, *ApJ*, 862, L25  
 Zhang, H., Li, X., Giannios, D., et al. 2020, *ApJ*, 901, 149

## Appendix A: Comparison of emission on milliarcsecond and arcsecond scales

The main beam sizes of the KVN single-dish and of the VLBA are largely different. This possibly causes the additional detection of extended jet structures in the KVN observations, leading to differences in polarization characteristics. To investigate, we checked the consistency between the two data sets. To do that, we compared the light curves obtained from the KVN and the VLBA at 43 GHz (Figure A.1). Each panel shows the observed values as in Figure 1. The total flux density  $S_I$  of the KVN is generally higher than that of the VLBA (by a factor of  $1.49 \pm 0.07$ ). However, the polarized flux density  $S_p$  is notably comparable (by a factor of  $1.02 \pm 0.07$ ). This indicates that the extended jet beyond the VLBA main beam size has a weak or negligible impact on  $S_p$ . Polarization angle depends on the ratio of the Stokes  $U$  and  $Q$  ( $\chi = 0.5 \tan^{-1}(U/Q)$ ), so  $\chi_{\text{obs}}$  may differ if there is a discrepancy between the Stokes parameters, even when the polarized flux density is comparable. From the comparison of the  $\chi_{\text{obs}}$  measurements, we found consistency between the two instruments. Therefore, we conclude that the obtained polarimetric features arise from the region within milliarcsecond-scale with negligible impact from the extended downstream jet. The polarization degree  $m_p$  is slightly lower in the KVN data due to its high  $S_I$ .

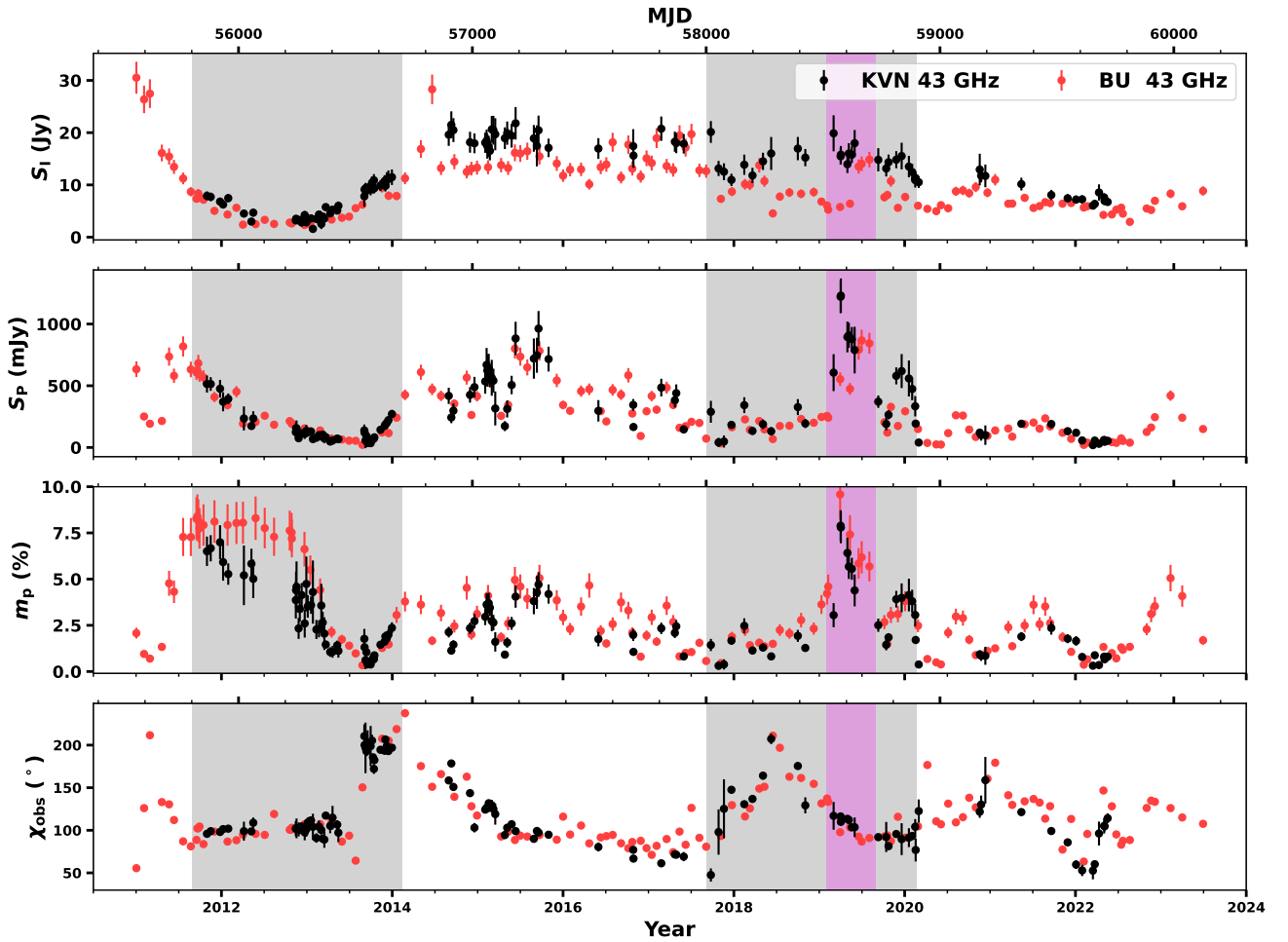


**Fig. A.1.** Comparison of the light curves at 43 GHz obtained from the KVN single-dish (black) and the VLBA (red). The flux density from the VLBA observations was estimated using the CLEAN models.

## Appendix B: Polarization angle and rotation measure of multiwavelength available epochs

We note that all Figures in Appendix B are available on [10.5281/zenodo.14967589](https://doi.org/10.5281/zenodo.14967589). Figure B.1 presents the results of only 4-frequency-available epochs. In the first (flux density, Jy) and second (spectral index,  $S_\nu \propto \nu^\alpha$ ) columns, the values of total and polarized emission densities are indicated by filled and open circles, respectively. The red dashed line in the second column indicates where  $\alpha = 0$ . In the third column, the polarization degree is shown on a fixed scale (0–12) in units of percent (%). In the fourth column, the obtained polarization angle ( $\chi_{\text{obs}}$ ) is shown with the RM-fit ( $\chi_0 = \chi + \text{RM} \lambda^2$ ) result as the red solid line in the squared wavelength ( $\lambda^2$ ) domain. The calculated RM value is noted in units of  $10^3 \text{ rad m}^{-2}$  in each panel. Although there are several epochs in which the linear fit well describes  $\chi_{\text{obs}}$  (i.e., constant RM), for some epochs, it cannot fit the observations. To investigate a possible frequency dependence of  $|\text{RM}|$ , we calculated RM at each adjacent frequency pair, as shown in the last column. The frequency in that column is the mean frequency of the pair ( $\nu_{\text{mean}}$ ). The red solid line indicates the fit result of  $|\text{RM}| \propto \nu^a$ , and the resultant  $a$  index is shown in each panel. The gray shaded area indicates the range of fitted RM in absolute value (i.e.,  $|\text{RM}_{\text{fit}}|$ ). Not only the

full-frequency-available  $|RM|$  but also three-frequency-available results are presented in Figure B.2. In many of the epochs,  $|RM|$  seems to increase as the pair frequency (i.e.,  $\nu_{\text{mean}}$ ) increases.

**Table B.1.** Observed polarization degrees and polarization angles from the KVN single-dish shown in Figure B.1.

Date	$m_p$ (%)				$\chi_{\text{obs}}$ (°)			
	22 GHz	43 GHz	86 GHz	129 GHz	22 GHz	43 GHz	86 GHz	129 GHz
2013-02-21	2.0 ± 0.2	2.3 ± 0.4	2.3 ± 0.2	0.6 ± 0.5	104.9 ± 3.0	104.2 ± 4.1	135.8 ± 4.3	107.7 ± 11.7
2013-03-03	1.8 ± 0.2	3.6 ± 1.2	1.5 ± 0.2	0.3 ± 0.4	105.1 ± 1.6	100.4 ± 3.0	126.4 ± 4.5	129.5 ± 10.1
2013-03-09	1.5 ± 0.3	2.7 ± 0.5	1.7 ± 0.4	0.7 ± 1.5	106.0 ± 3.6	90.2 ± 4.1	129.8 ± 10.1	121.4 ± 20.5
2013-03-16	1.4 ± 0.7	2.0 ± 1.0	0.3 ± 0.2	1.3 ± 0.4	104.1 ± 9.6	89.0 ± 9.1	99.0 ± 12.5	117.0 ± 12.1
2015-10-31	2.5 ± 0.2	4.2 ± 0.2	4.7 ± 0.1	4.9 ± 0.5	94.3 ± 1.5	94.8 ± 0.5	80.8 ± 0.4	94.2 ± 2.4
2016-05-31	1.7 ± 0.2	1.8 ± 0.3	4.2 ± 1.4	4.2 ± 2.7	91.5 ± 1.4	80.5 ± 2.6	77.7 ± 20.8	78.4 ± 27.7
2016-10-28	1.8 ± 0.1	1.1 ± 0.1	1.3 ± 0.1	1.3 ± 0.2	78.0 ± 0.9	66.7 ± 0.9	66.8 ± 2.9	63.6 ± 5.0
2017-02-24	1.9 ± 0.1	2.3 ± 0.1	1.8 ± 0.9	1.9 ± 0.4	67.1 ± 0.8	61.2 ± 1.1	31.9 ± 13.2	50.6 ± 6.7
2017-09-24	1.0 ± 0.4	1.4 ± 0.3	1.8 ± 1.2	2.8 ± 2.4	67.0 ± 7.7	47.5 ± 7.0	63.2 ± 27.6	44.5 ± 23.9
2017-10-27	0.5 ± 0.1	0.3 ± 0.3	1.1 ± 0.2	1.4 ± 0.1	85.4 ± 1.2	97.9 ± 19.8	154.8 ± 5.3	120.7 ± 3.6
2017-11-19	0.3 ± 0.2	0.4 ± 0.4	0.8 ± 0.6	2.9 ± 0.9	175.1 ± 16.4	125.2 ± 25.5	129.6 ± 25.3	128.4 ± 12.8
2018-11-02	1.2 ± 0.1	1.3 ± 0.1	2.9 ± 0.9	2.5 ± 1.6	166.5 ± 3.5	129.3 ± 8.4	152.1 ± 19.6	118.8 ± 20.9
2019-03-03	3.4 ± 0.4	3.1 ± 0.5	3.7 ± 0.8	5.0 ± 0.7	124.4 ± 21.2	116.9 ± 12.9	108.2 ± 12.4	112.2 ± 3.9
2019-04-02	5.7 ± 0.1	7.9 ± 0.1	9.1 ± 0.5	10.3 ± 0.9	116.0 ± 0.7	116.2 ± 0.9	92.4 ± 1.1	112.6 ± 2.0
2019-04-03	5.8 ± 0.1	7.8 ± 0.1	8.1 ± 0.5	10.7 ± 0.8	113.8 ± 1.5	109.9 ± 1.9	118.5 ± 1.4	111.7 ± 2.1
2019-05-01	5.3 ± 0.2	6.4 ± 0.3	7.8 ± 0.1	9.7 ± 0.4	117.2 ± 2.3	113.4 ± 1.9	110.7 ± 4.1	104.7 ± 3.4
2019-05-20	4.4 ± 0.1	5.6 ± 0.1	4.3 ± 0.6	6.0 ± 0.6	114.1 ± 0.4	103.5 ± 0.7	94.3 ± 3.9	101.2 ± 3.0
2019-06-01	3.9 ± 0.3	4.4 ± 0.6	5.3 ± 1.2	5.7 ± 1.4	105.7 ± 4.9	103.6 ± 8.7	90.9 ± 7.0	109.1 ± 4.0
2019-10-14	1.6 ± 0.1	1.4 ± 0.2	1.5 ± 0.6	2.3 ± 1.1	110.8 ± 14.2	92.1 ± 17.1	99.4 ± 10.9	86.0 ± 11.0
2019-11-26	2.3 ± 0.3	3.9 ± 0.1	4.7 ± 0.7	5.1 ± 1.6	101.7 ± 11.2	95.6 ± 3.0	97.0 ± 5.2	116.7 ± 8.2
2019-12-19	2.3 ± 0.2	4.0 ± 0.6	3.7 ± 0.4	4.9 ± 0.4	97.2 ± 8.6	89.6 ± 18.6	105.6 ± 3.3	112.5 ± 5.9
2020-01-19	2.7 ± 0.6	4.1 ± 0.7	4.1 ± 0.5	4.6 ± 0.5	115.7 ± 16.3	91.3 ± 10.7	100.1 ± 3.4	106.8 ± 3.5
2020-02-02	2.8 ± 0.3	3.8 ± 0.4	4.5 ± 0.8	5.1 ± 1.0	112.6 ± 8.8	93.3 ± 4.2	99.8 ± 5.0	105.5 ± 3.4
2020-11-23	0.7 ± 0.1	0.9 ± 0.3	2.0 ± 0.4	1.8 ± 0.7	117.0 ± 21.9	130.2 ± 8.5	116.9 ± 3.9	119.4 ± 13.4
2020-12-11	0.3 ± 0.4	0.9 ± 0.6	1.8 ± 0.4	2.6 ± 0.9	148.3 ± 49.2	158.8 ± 16.1	114.9 ± 5.3	107.1 ± 9.5
2021-05-14	1.5 ± 0.1	2.0 ± 0.1	0.7 ± 0.3	1.6 ± 0.9	132.2 ± 2.6	121.3 ± 0.7	90.9 ± 13.8	73.3 ± 11.3
2021-09-19	4.7 ± 3.0	2.4 ± 0.2	1.6 ± 0.6	3.1 ± 2.6	86.5 ± 13.7	99.1 ± 2.6	88.7 ± 10.2	97.5 ± 24.7
2022-01-29	0.9 ± 0.1	0.8 ± 0.1	1.5 ± 0.5	2.0 ± 0.9	55.8 ± 10.5	52.9 ± 5.0	30.8 ± 7.0	47.5 ± 23.5
2022-04-11	0.8 ± 0.1	0.4 ± 0.1	2.2 ± 0.8	1.6 ± 2.5	65.9 ± 13.9	96.2 ± 11.0	168.3 ± 8.1	107.8 ± 34.3
2022-05-03	1.0 ± 0.1	0.8 ± 0.1	1.6 ± 0.3	2.0 ± 1.7	86.3 ± 12.5	105.2 ± 5.5	122.7 ± 1.8	115.9 ± 34.9
2022-05-18	1.0 ± 0.1	0.8 ± 0.1	1.9 ± 0.6	2.1 ± 1.3	79.2 ± 12.3	114.2 ± 2.0	139.1 ± 8.2	140.9 ± 20.3

**Table B.2.** Obtained values of the Faraday rotation measure and  $a$  index. The selected epochs are the same as those listed in Table B.1

Date	RM <sub>fit</sub>	RM ( $10^3$ rad m <sup>-2</sup> )			$a$ ( $ \text{RM}  \propto \nu^a$ )
		22–43 GHz	43–86 GHz	86–129 GHz	
2013-02-21	$-1.42 \pm 1.99$	$0.1 \pm 0.6$	$-15.1 \pm 2.8$	$72.7 \pm 32.3$	$3.96 \pm 0.98$
2013-03-03	$-2.00 \pm 1.64$	$0.6 \pm 0.4$	$-12.4 \pm 2.6$	$-8.0 \pm 28.6$	$3.30 \pm 1.22$
2013-03-09	$-1.54 \pm 2.32$	$2.0 \pm 0.7$	$-18.9 \pm 5.2$	$21.7 \pm 59.1$	$3.09 \pm 0.45$
2013-03-16	$-0.22 \pm 1.70$	$1.9 \pm 1.7$	$-4.8 \pm 7.4$	$-46.6 \pm 45.0$	$2.23 \pm 1.00$
2015-10-31	$0.57 \pm 0.92$	$-0.1 \pm 0.2$	$6.7 \pm 0.3$	$-34.6 \pm 6.2$	$3.77 \pm 0.76$
2016-05-31	$1.33 \pm 0.09$	$1.4 \pm 0.4$	$1.3 \pm 10.1$	$-1.9 \pm 89.7$	$0.76 \pm 0.63$
2016-10-28	$1.29 \pm 0.19$	$1.4 \pm 0.2$	$-0.0 \pm 1.5$	$8.3 \pm 15.0$	$0.75 \pm 1.52$
2017-02-24	$2.33 \pm 1.56$	$0.7 \pm 0.2$	$14.0 \pm 6.4$	$-48.2 \pm 38.3$	$3.62 \pm 0.47$
2017-09-24	$1.46 \pm 1.29$	$2.5 \pm 1.3$	$-7.5 \pm 13.6$	$48.5 \pm 94.4$	$2.08 \pm 0.51$
2017-10-27	$-4.73 \pm 2.97$	$-1.6 \pm 2.5$	$-27.2 \pm 9.8$	$88.0 \pm 16.5$	$2.93 \pm 0.55$
2017-11-19	$4.71 \pm 1.04$	$6.3 \pm 3.9$	$-2.1 \pm 17.2$	$3.2 \pm 73.2$	$1.12 \pm 1.38$
2018-11-02	$3.31 \pm 2.15$	$4.7 \pm 1.2$	$-10.9 \pm 10.2$	$86.2 \pm 74.0$	$1.62 \pm 0.72$
2019-03-03	$1.35 \pm 0.38$	$0.9 \pm 3.2$	$4.2 \pm 8.6$	$-10.5 \pm 33.7$	$2.04 \pm 0.12$
2019-04-02	$1.14 \pm 1.47$	$-0.0 \pm 0.1$	$11.4 \pm 0.7$	$-52.3 \pm 5.9$	$3.76 \pm 0.95$
2019-04-03	$-0.06 \pm 0.55$	$0.5 \pm 0.3$	$-4.1 \pm 1.1$	$17.7 \pm 6.6$	$2.99 \pm 0.10$
2019-05-01	$0.91 \pm 0.43$	$0.5 \pm 0.4$	$1.3 \pm 2.2$	$15.4 \pm 13.8$	$2.65 \pm 1.07$
2019-05-20	$1.57 \pm 0.48$	$1.4 \pm 0.1$	$4.4 \pm 1.9$	$-18.0 \pm 12.9$	$1.87 \pm 0.24$
2019-06-01	$0.48 \pm 1.12$	$0.3 \pm 1.3$	$6.1 \pm 5.3$	$-47.2 \pm 20.8$	$4.08 \pm 0.15$
2019-10-14	$1.88 \pm 0.83$	$2.4 \pm 2.8$	$-3.5 \pm 9.7$	$34.7 \pm 40.0$	$1.80 \pm 1.14$
2019-11-26	$-0.44 \pm 1.39$	$0.8 \pm 1.5$	$-0.6 \pm 2.9$	$-51.1 \pm 25.1$	$8.47 \pm 5.08$
2019-12-19	$-0.99 \pm 1.28$	$1.0 \pm 2.6$	$-7.7 \pm 9.1$	$-17.8 \pm 17.5$	$2.36 \pm 0.45$
2020-01-19	$1.36 \pm 1.17$	$3.1 \pm 2.5$	$-4.2 \pm 5.4$	$-17.5 \pm 12.7$	$1.00 \pm 0.76$
2020-02-02	$1.10 \pm 0.92$	$2.5 \pm 1.2$	$-3.1 \pm 3.1$	$-14.7 \pm 15.5$	$0.89 \pm 0.67$
2020-11-23	$-0.26 \pm 0.91$	$-1.7 \pm 3.0$	$6.4 \pm 4.5$	$-6.6 \pm 36.1$	$1.72 \pm 0.44$
2020-12-11	$3.23 \pm 2.90$	$-1.3 \pm 6.6$	$21.0 \pm 8.1$	$20.2 \pm 28.1$	$1.77 \pm 1.26$
2021-05-14	$4.66 \pm 2.25$	$1.4 \pm 0.3$	$14.6 \pm 6.6$	$45.4 \pm 46.2$	$3.21 \pm 0.28$
2021-09-19	$-0.76 \pm 0.75$	$-1.6 \pm 1.8$	$5.0 \pm 5.0$	$-22.7 \pm 69.1$	$1.74 \pm 0.30$
2022-01-29	$1.47 \pm 1.27$	$0.4 \pm 1.5$	$10.6 \pm 4.1$	$-43.1 \pm 63.4$	$3.57 \pm 0.74$
2022-04-11	$-6.64 \pm 4.22$	$-3.9 \pm 2.3$	$-34.5 \pm 6.5$	$156.4 \pm 91.1$	$3.13 \pm 0.09$
2022-05-03	$-3.16 \pm 0.69$	$-2.4 \pm 1.7$	$-8.4 \pm 2.8$	$17.6 \pm 90.4$	$1.82 \pm 0.04$
2022-05-18	$-5.85 \pm 0.89$	$-4.4 \pm 1.6$	$-11.9 \pm 4.0$	$-4.5 \pm 56.5$	$1.37 \pm 0.26$



Appendix C: VLBA 43 GHz images during polarization flare

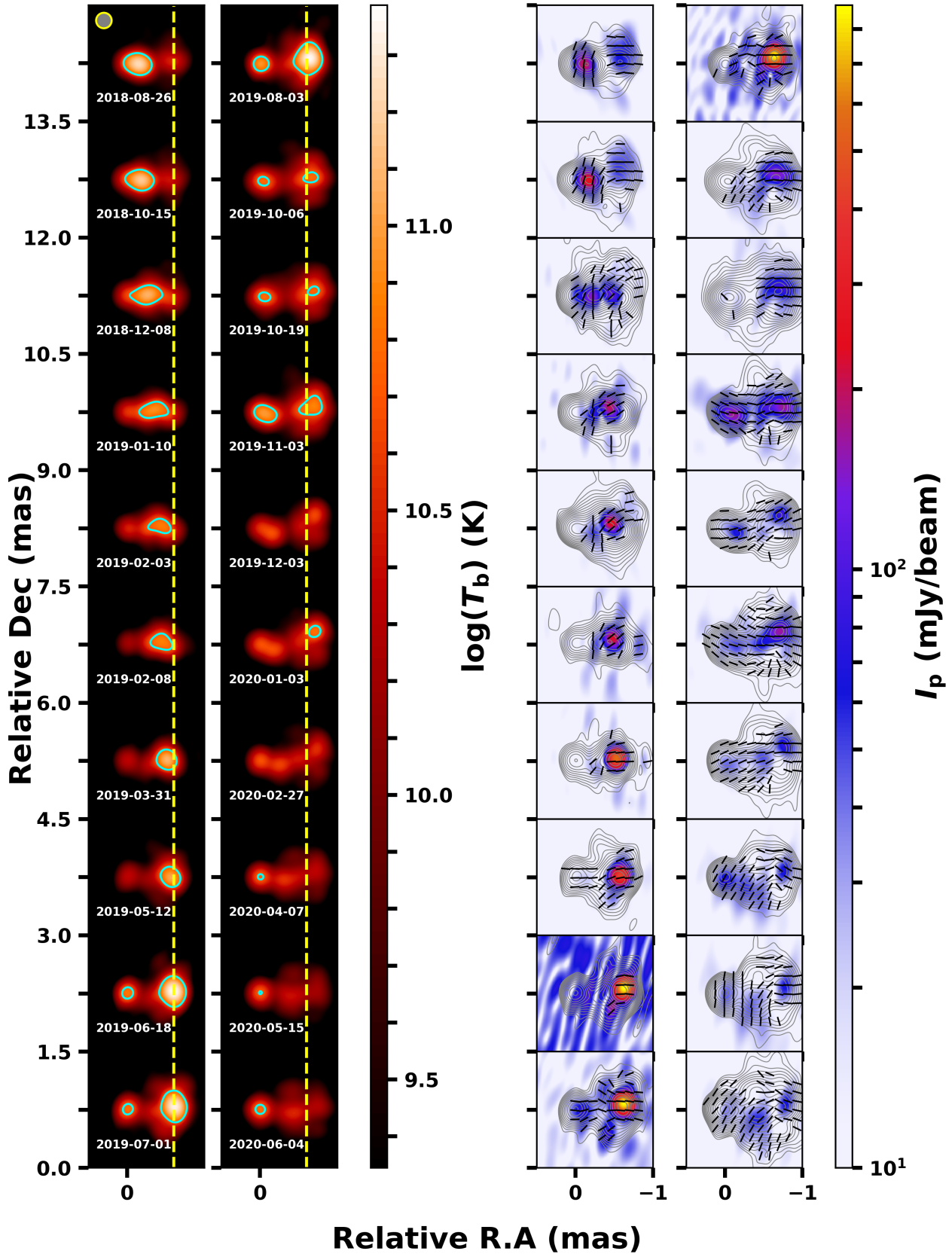


Fig. C.1. Same as in Figure 2, but for the period around the flare in 2019.